International Journal of Solids and Structures 308 (2025) 113128

Contents lists available at ScienceDirect

International Journal of Solids and Structures

journal homepage: www.elsevier.com/locate/ijsolstr

Ductile failure by strain localisation: A computational study of materials and structures subjected to highly non-proportional load histories

Martin Kristoffersen *, David Morin, Tore Børvik, Odd Sture Hopperstad

Structural Impact Laboratory (SIMLab), Department of Structural Engineering, Norwegian University of Science and Technology (NTNU), Trondheim, Norway

ARTICLE INFO

Keywords:
Ductile failure
Unit cell analysis
Non-proportional loading
Strain localisation

ABSTRACT

Ductile failure by the onset of strain localisation after non-proportional load paths is investigated herein by using the imperfection version of the strain localisation theory. A computational framework assuming a planar, porous imperfection band inside a homogeneous solid was used to investigate ductile failure as caused by void nucleation, growth, and coalescence. The localisation analysis framework was calibrated based on a single uniaxial tension test and finite element simulations thereof. Despite the somewhat frugal calibration, the localisation analyses successfully reproduced experimentally measured macroscopic fracture strains from notched tension tests and notched compression–tension tests. The method was subsequently applied to a structural problem involving large deformations and complex load paths, and the results show great promise for future work.

1. Introduction

Ductile fracture in solids is a phenomenon that has been studied for several decades using experimental, theoretical and numerical approaches. It is well established that increasing stress triaxiality T, exponentially reduces the failure strain of ductile metals (Hancock and Mackenzie, 1976; Hancock and Brown, 1983; Bao and Wierzbicki, 2004). Void nucleation, growth and subsequent coalescence can be explained by theoretical models predicting the observed increased void growth with increased stress triaxiality, exemplified by the work of Rice and Tracey (1969) and Gurson (1977). In addition to the stress triaxiality T, the Lode parameter L affects the ductility for low to medium levels of T (Bao and Wierzbicki, 2004; Barsoum and Faleskog, 2007). While notched specimens allow control over the initial value of T experimentally, the Lode parameter is particularly elusive to control in physical tests. The effects of L are therefore difficult to quantify through testing alone. Thus, finite element (FE) simulations have become a crucial instrument in understanding the micromechanics of ductile failure through the use of unit cell analyses. This approach involves modelling a small representative volume, or unit cell, of the material. This unit cell is designed to represent the microstructure and material properties relevant to the behaviour of interest, such as plasticity and void growth.

Early unit cell approaches considered an axisymmetric approximation with periodic boundary conditions (Tvergaard, 1982; Koplik and Needleman, 1988). As the computational power increased, this approach was extended to full three-dimensional unit cells (Barsoum and Faleskog, 2011; Tekoglu et al., 2015; Dæhli et al., 2018; Vishwakarma and Keralavarma, 2019; Chouksey and Basu, 2021). Parameters such as plastic anisotropy, void volume fraction, void shape and distribution, stress states, and load path may be easily controlled in unit cell analyses, allowing detailed investigations of their effects. 3D unit cells are, however, computationally expensive, particularly if wide ranges of parameters are to be explored. With respect to CPU cost, the strain localisation (or imperfection) analysis approach following Marciniak and Kuczynski (1967) and Rice (1976) is far less costly. A total of 1 600 different stress states were analysed by Morin et al. (2018) in less than 10 min in parallel on 48 CPUs, whereas a 3D unit cell approach as laid out by Dunand and Mohr (2014) covering the same stress states would consume 17 years of CPU time assuming 12 CPUs dedicated to each unit cell analysis. The basic assumption of the localisation analysis approach is that of a homogeneously deformed solid containing a thin planar band with a small imperfection. The material outside the band is modelled by a different constitutive relation than the material inside, where some kind of softening mechanism (temperature, void growth/nucleation, damage, etc.) is introduced to represent the (relative) imperfection. As the material deforms homogeneously and sufficiently, all deformation will eventually be constrained to the imperfection band, thereby indicating the onset of localisation. The results from the localisation analyses have been shown to capture the same qualitative features as both experiments and unit cells for proportional loading. The imperfection variant of the localisation approach, as opposed to the bifurcation variant, thus accounts for the

* Corresponding author.
E-mail address: martin.kristoffersen@ntnu.no (M. Kristoffersen).

https://doi.org/10.1016/j.ijsolstr.2024.113128
Received 16 February 2024; Received in revised form 5 October 2024; Accepted 30 October 2024
Available online 19 November 2024

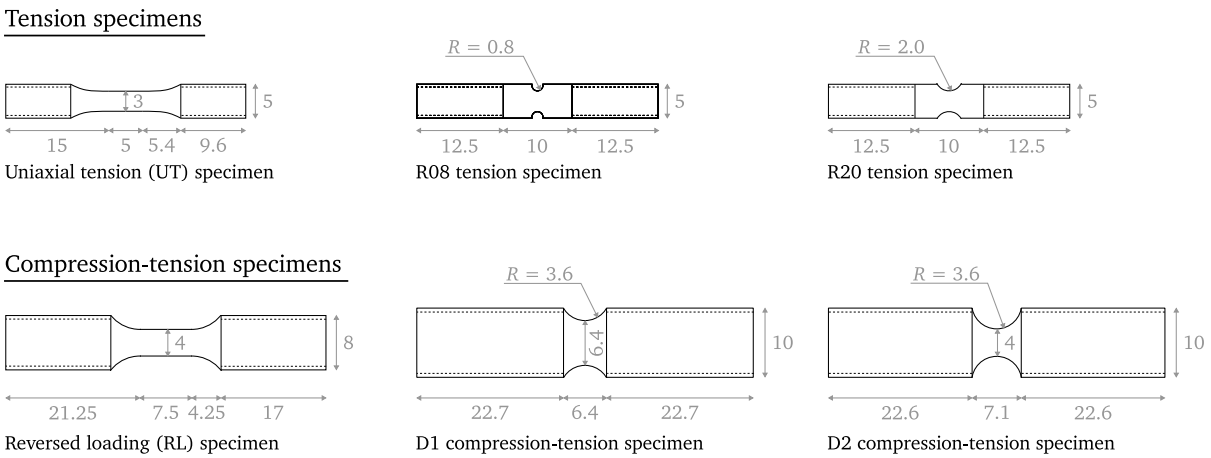

Fig. 1. All six axisymmetric specimen geometries (measurements in mm) used in this study. The various specimens will generally be referred to by the short name in this figure.

entire deformation history of the material. The bifurcation version is, however, even less costly and has been implemented to work in-situ in a finite element framework (Erice et al., 2020; Bergo et al., 2021; Espeseth et al., 2021).

In general, load paths in materials and structures subjected to extreme loads and large deformations are not proportional. Many experimental studies investigate the load path effect – Ludley and Drucker (1960) made bent-beam specimens which created a compressive zone in the nook of the specimen. The bent specimens were subsequently straightened, thereby imposing a tensile load on the compressed side and a ductile-to-brittle transition was observed. A similar experimental approach was adopted by Manes et al. (2012), while Bao and Wierzbicki (2004) used notched and cylindrical specimens for compression testing of a 2024-T351 aluminium alloy, in which fracture initiated by shear in the equatorial area. For the same alloy, combined tension/compression/torsion experiments on tubular specimens were carried out by Papasidero et al. (2015). Their experimental results indicated that precompression may increase the ductility of the alloy. Steel specimens compressed to various strain levels before being stretched to failure in tension showed a clear reduction in strain to failure relative to the initial geometry (Enami, 2005; Kristoffersen et al., 2013b), and a transition to brittle or shear fracture for the highest compression levels. A similar study on 6xxx aluminium alloys found that the fracture strain after compression was dependent on the strength and microstructure of the alloy in question (Frodal et al., 2017). Compression–tension tests by Marcadet and Mohr (2015) on DP780 steel sheets indicate that the strain to failure may increase for precompression levels up to 13 %.

Numerous studies have thus demonstrated that failure strains obtained from non-proportional load paths differ distinctly from those arising from proportional loading (Basu and Benzerga, 2015; Yu et al., 2016; Dæhli et al., 2016; Thomas et al., 2016; He et al., 2020). Additionally, equal time-weighted average stress triaxialities via different load paths do not necessarily produce a unique strain to failure (Benzerga et al., 2012). Tensile prestrain up to 5 % and 10 % with $T = 1/3$ on axisymmetric unit cells with an initially spherical void has been shown to reduce the strain to coalescence for subsequent tension with $T = 1$ (Zhang and Skallerud, 2010), and the effect increases for increasing T. When a particle is included in the void, compressive prestrain has a similar effect (Kristoffersen et al., 2016a). Further, the strain to failure after a change in T or L depends nonlinearly on the level of prestrain before the change (Chouksey and Keralavarma, 2022). Porous plasticity models and uncoupled phenomenological damage models have been able to qualitatively capture prestrain effects numerically (Oh et al., 2007; Thomas et al., 2016; Kristoffersen et al., 2018b). Localisation (or imperfection) analyses as laid out by Rice (1976) is a computationally efficient tool which may predict localisation accurately (Morin et al., 2018), and has been applied successfully to some cases of non-proportional loading as well (Morin et al., 2019).

This study has two main goals. The first is to validate the localisation analysis approach across a range of monotonic and non-proportional loads for which good experimental data is available (Kristoffersen et al., 2013b, 2016a). While the term applies to general path changing loading conditions, "non-proportional loading" is typically applied within the positive stress triaxiality regime. Here, we extend the analyses to cases with severe compressive strains preceding tension. Six different specimen geometries as shown in Fig. 1 are employed. The second goal is to examine whether the localisation approach is viable for a structural problem involving complex load paths not covered by the material tests. The results suggest that the localisation analysis is a very good predictor of fracture initiation for the load cases considered given an adequate void evolution formulation.

2. Simulation strategy

An overview of the simulation strategy used in this study is given in Fig. 2. Part ❶ consists of previously published material tests (Kristoffersen et al., 2013b, 2016a) providing macroscopic stress–strain data for various specimen geometries and load paths. The material test results are used for calibration and validation of the constitutive model in part ❷ and are not presented in a distinct section but invoked when needed as in for instance Fig. 3. All material tests were conducted with perpendicular lasers continuously measuring the minimum cross-section diameters throughout each test, thereby by enabling calculation of the net axial stress and logarithmic strain beyond necking all the way to failure, albeit as an average across the minimum specimen cross-section.

Part ❷ describes the metal plasticity model, which is used in FE simulations of the material tests and in the matrix of the unit cell analyses in part ❸ and *outside* the imperfection band in the localisation analyses. The FE unit cell analyses provide data for calibration of the porous plasticity model, which constitutes part ❹. This constitutive model is used for the material *inside* the imperfection band in the localisation analyses (part ❺). Finally, the localisation analyses are applied to an array of material tests and a structural problem involving large deformations and complex load paths.

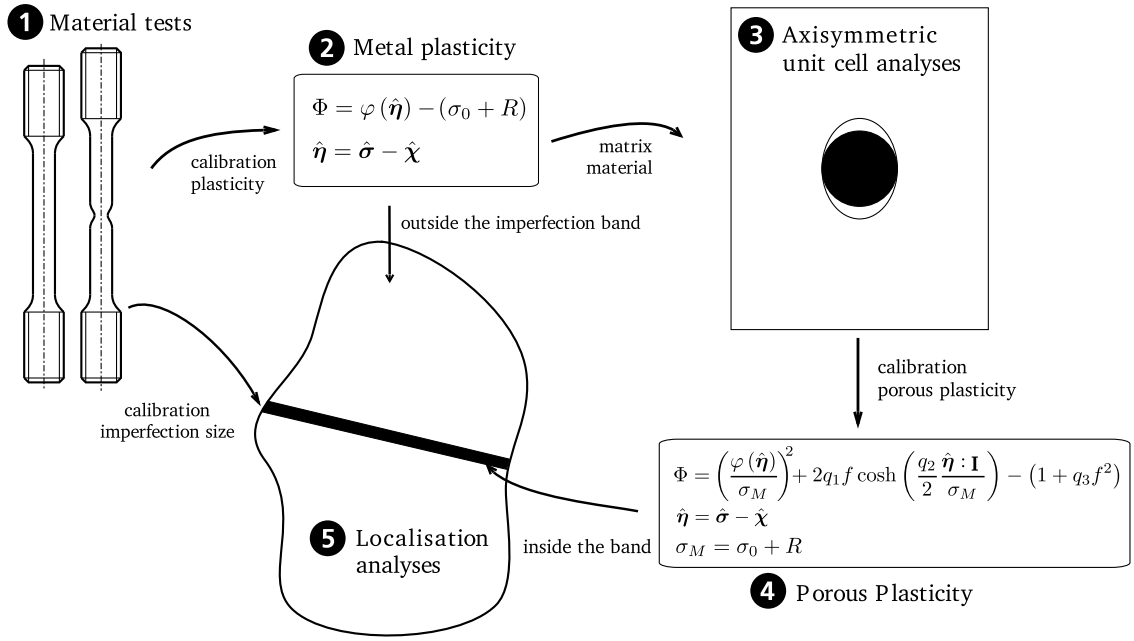

Fig. 2. Overall description of the simulation and calibration approach.

3. Material behaviour

3.1. Description of the X65 steel

The material used in this study is an X65 grade steel, a material widely used in pipelines conveying oil and/or gas. Based on 12 uniaxial tension (UT) tests, the yield stress (and standard deviation) was 478 ± 15 MPa, the ultimate tensile strength 572 ± 14 MPa, and the fracture strain $\varepsilon_f = 1.61 \pm 0.03$. The macroscopic fracture strain was defined as $\varepsilon_f = \ln(A_0/A_f)$, where A_0 is the initial cross-sectional area of the specimen and A_f the area at fracture, obtained by a micrometer. This measure is, however, an average across the cross-section and does not account for local strain variations. Bridgman's analysis (Bridgman, 1943; Hill, 1950) and experimental observations (Ghahremaninezhad and Ravi-Chandar, 2011) have shown that a nonuniform distribution of strain arises in tensile specimens due to high stress triaxiality at the centre of the neck. Here, we will use the experimentally measured macroscopic fracture strain ε_f to identify the point from which to extract the equivalent plastic strain in FE analyses (presented in detail later).

Further, the Young's modulus of the X65 steel is $E = 208\,000$ MPa, and the material has a ferritic grain structure with grain size ≤ 10 micrometer (Kristoffersen et al., 2013b). Previous work has shown that for engineering purposes the material may be considered homogeneous and isotropic, and it exhibits a moderate strain rate sensitivity of the flow stress, while the fracture strain is unaffected by the strain rate (Kristoffersen et al., 2014). All tests herein were conducted quasi-statically at room temperature, so any strain rate sensitivity and temperature effects were therefore omitted in the models. Perpendicular lasers were used to measure the minimum diameters D_x and D_y of the specimen continuously throughout the tests, and the material showed no signs of anisotropy. These measurements also give the current minimum cross-sectional area $A = (\pi/4)D_x D_y$, which with synchronised measurements of the force F, provide the net axial stress σ and the logarithmic strain ε, defined by

$$\sigma = \frac{F}{A}, \qquad \varepsilon = \ln\left(\frac{A_0}{A}\right) \tag{1}$$

The stress–strain curves arising from Eq. (1) are then used as target curves when calibrating the material constants in the metal plasticity model described next.

3.2. Metal plasticity

The metal plasticity model assumes small elastic deformations, while the plastic deformations and the rotations are allowed to be finite. A corotational stress formulation is used to handle large rotations. Yielding, plastic flow, and hardening are governed by the von Mises yield criterion, the associated flow rule and combined nonlinear isotropic and kinematic hardening rules.

The corotated stress tensor $\hat{\boldsymbol{\sigma}}$ and the corotated rate-of-deformation tensor $\hat{\mathbf{D}}$ are defined by

$$\hat{\boldsymbol{\sigma}} = \mathbf{R}^{\mathrm{T}} \cdot \boldsymbol{\sigma} \cdot \mathbf{R}, \qquad \hat{\mathbf{D}} = \mathbf{R}^{\mathrm{T}} \cdot \mathbf{D} \cdot \mathbf{R} \tag{2}$$

where $\boldsymbol{\sigma}$ and $\mathbf{D}$ are the Cauchy stress and rate-of-deformation tensors, respectively, with respect to a fixed global coordinate system. $\mathbf{R}$ is an orthogonal tensor ($\mathbf{R}^{\mathrm{T}} = \mathbf{R}^{-1}$) defining the change of base vectors between the fixed global axes and the local corotational material axes. $\mathbf{R}$ has an initial value equal to the second order identity tensor $\mathbf{I}$ and changes with the spin tensor $\mathbf{W}$ so that $\dot{\mathbf{R}} = \mathbf{W} \cdot \mathbf{R}$. The rate of $\hat{\boldsymbol{\sigma}}$ is then

$$\dot{\hat{\boldsymbol{\sigma}}} = \mathbf{R}^{\mathrm{T}} \left(\mathbf{W}^{\mathrm{T}}\boldsymbol{\sigma} + \dot{\boldsymbol{\sigma}} + \boldsymbol{\sigma}\mathbf{W}\right) \mathbf{R} \tag{3}$$

An additive decomposition of $\hat{\mathbf{D}}$ is assumed,

$$\hat{\mathbf{D}} = \hat{\mathbf{D}}_{\mathrm{el}} + \hat{\mathbf{D}}_{\mathrm{pl}} \tag{4}$$

where $\hat{\mathbf{D}}_{\mathrm{el}}$ and $\hat{\mathbf{D}}_{\mathrm{pl}}$ are the elastic and plastic parts of $\hat{\mathbf{D}}$, respectively. The rate form of the isotropic linear elastic relation is expressed in terms of $\hat{\mathbf{D}}_{\mathrm{el}}$ as

$$\dot{\hat{\boldsymbol{\sigma}}} = \frac{E}{1+\nu}\hat{\mathbf{D}}'_{\mathrm{el}} + \frac{E}{3(1-2\nu)}\mathrm{tr}\left(\hat{\mathbf{D}}_{\mathrm{el}}\right)\mathbf{I} \tag{5}$$

where ν is the Poisson ratio, and the prime in $\hat{\mathbf{D}}'_{\mathrm{el}}$ indicates the deviatoric part, which means $\hat{\mathbf{D}}'_{\mathrm{el}} = \hat{\mathbf{D}}_{\mathrm{el}} - \frac{1}{3}\mathrm{tr}\left(\hat{\mathbf{D}}_{\mathrm{el}}\right)\mathbf{I}$.

The von Mises equivalent stress σ_{eq} with respect to the backstress is defined in terms of the corotated effective stress tensor $\hat{\boldsymbol{\eta}} = \hat{\boldsymbol{\sigma}} - \hat{\boldsymbol{\chi}}$, viz.

$$\sigma_{\text{eq}} = \varphi(\hat{\boldsymbol{\eta}}) = \sqrt{\frac{3}{2}\,\hat{\boldsymbol{\eta}}' : \hat{\boldsymbol{\eta}}'} \tag{6}$$

with $\hat{\boldsymbol{\chi}}$ being the corotated backstress tensor. The yield function Φ is given by

$$\Phi(\hat{\boldsymbol{\eta}}, R) = \varphi(\hat{\boldsymbol{\eta}}) - \left(\sigma_0 + R\right) \tag{7}$$

in which σ_0 is the initial yield stress. The variable $R = \sum_i R_i$ represents the isotropic strain hardening, and is a sum of multiple components R_i with evolution equations (Voce, 1948)

$$\dot{R}_i = \theta_{Ri}\left(1 - \frac{R_i}{Q_{Ri}}\right)\dot{p} \tag{8}$$

where $\dot{p}$ is the equivalent plastic strain rate, and θ_{Ri} and Q_{Ri} are the strain hardening parameters. In a similar fashion, the corotated backstress tensor $\hat{\boldsymbol{\chi}}$, which governs the kinematic hardening, is decomposed into multiple parts $\hat{\boldsymbol{\chi}} = \sum_i \hat{\boldsymbol{\chi}}_i$. The evolution equations of the partial backstress tensors $\hat{\boldsymbol{\chi}}_i$ are given by Armstrong and Frederick (1966)

$$\dot{\hat{\boldsymbol{\chi}}}_i = \theta_{\chi i}\left(\frac{\hat{\boldsymbol{\eta}}}{\varphi(\hat{\boldsymbol{\eta}})} - \frac{\hat{\boldsymbol{\chi}}_i}{Q_{\chi i}}\right)\dot{p} \tag{9}$$

where $\theta_{\chi i}$ and $Q_{\chi i}$ are the kinematic hardening parameters.

The associated flow rule describes the plastic flow, i.e.,

$$\hat{\mathbf{D}}_{\text{pl}} = \dot{\lambda}\,\frac{\partial \Phi}{\partial \hat{\boldsymbol{\eta}}} \tag{10}$$

with $\dot{\lambda}$ being the plastic parameter, and the equivalent plastic strain p is obtained by integrating in time from 0 to t,

$$p = \int_0^t \dot{\lambda}\,\mathrm{d}\tau = \int_0^t \dot{p}\,\mathrm{d}\tau \tag{11}$$

Finally, the loading–unloading conditions are

$$\Phi \le 0 \qquad \dot{\lambda} \ge 0 \qquad \Phi\dot{\lambda} = 0 \tag{12}$$

3.3. Calibration of metal plasticity constants

To calibrate the material constants in the metal plasticity model, an axisymmetric FE model was created using ABAQUS/Standard (SIMULIA, 2021). The UT and RL specimens from Fig. 1 were meshed with fully integrated linear 4-node elements with side lengths approximately 0.1 mm. Possible volumetric locking is handled by "selective reduced integration", whereby the volumetric change in the integration points are replaced by the average volume change of the element (SIMULIA, 2021). The macroscopic stress–strain curves from the FE models were obtained in the same manner as in the experiments through Eq. (1) from the numerical reaction forces and the minimum specimen diameter, providing a direct comparison in this inverse modelling approach. The RL specimen was used to calibrate the kinematic hardening parameters as laid out in Kristoffersen et al. (2016a) while the UT specimen provides additional information for the isotropic hardening. Two terms for both the isotropic and kinematic hardening provide sufficient accuracy.

The resulting macroscopic stress–strain curve (dashed red) for the UT specimen is plotted in Fig. 3(a) along with the experimental data (solid black), thus confirming a good fit. Next, validation simulations of the notched tension specimens R08 and R20 – not used for calibration – were run. Different notch geometries give different stress triaxialities T in each specimen, resulting in different macroscopic failure strains ε_{f}. The simulation results were then compared with corresponding experimental data and the fit is good for all specimens even though only the UT specimen was used for calibration (see Fig. 3(a)). The D1 and D2 samples subjected to compression–tension loading (Kristoffersen et al., 2013b, 2016a) were used for further validation, and the results are shown in Fig. 3(b) and (c), respectively. In addition to tension only, the D1 specimens were compressed to logarithmic strain levels of 0.1, 0.2, 0.3 and 0.4, and the D2 specimens to 0.4, 0.6, 0.8 and 0.9 before being stretched to failure in tension. Again, the overall fit between the simulations and the experiments is very good with the exception of the work-hardening stagnation observed after load reversal as highlighted in Fig. 3(c), which also indicates the initial point of yielding, load reversal, and re-yielding – points used for calibrating the kinematic hardening using the procedure from (Kristoffersen et al., 2016a). Work-hardening stagnation increased with increasing pre-compression, and requires special attention when modelling if it is to be accurately captured. Still, for the purposes of this study, the model is deemed to be of sufficient accuracy.

Table 1
Material constants for the metal plasticity model with combined isotropic and kinematic hardening.

Elasticity and density	E [MPa]	ν [–]	σ_0 [MPa]	ρ_{X65} [kg/m^3]
	208 000	0.33	330.0	7 800
Isotropic hardening	Q_{R1} [MPa]	θ_{R1} [MPa]	Q_{R2} [MPa]	θ_{R2} [MPa]
	400.0	330.7	50.5	1 752.0
Kinematic hardening	$Q_{\chi 1}$ [MPa]	$\theta_{\chi 1}$ [MPa]	$Q_{\chi 2}$ [MPa]	$\theta_{\chi 2}$ [MPa]
	126.2	115 600.0	101.1	2 220.0
Porous plasticity	q_1 [–]	q_2 [–]	q_3 [–]	
	1.000	1.116	1.000	

Three different strain hardening versions for the metal plasticity model were used: (i) combined isotropic and kinematic hardening, (ii) purely isotropic hardening, (iii) purely kinematic hardening. Cases (i) and (ii) are illustrated in Fig. 4, where (a) shows the combined hardening decomposed into isotropic and kinematic parts, illustrating that the kinematic hardening dominates for low levels of plastic strain, and saturates quickly. Part (b) in Fig. 4 shows that the combined hardening model and the purely isotropic hardening model are both able to describe the same macroscopic stress–strain curve for proportional loading. It is possible to achieve the same result as in Fig. 4(b) with a purely kinematic hardening model as well (Mear and Hutchinson, 1985), but this is omitted for brevity. The material constants for the combined hardening model, including the mass density ρ_{X65}, are listed in Table 1. The values are the same as obtained in Kristoffersen et al. (2016a), with the exception of Q_{R1} which was modified to improve the fit for large strain values.

3.4. Porous plasticity

The material inside the imperfection band in the localisation analyses is described by a porous plasticity model. A requirement for localisation in the form of a material instability as defined by Rice (1976) is a softening mechanism, so in the porous plasticity model softening is introduced by nucleation and growth of voids under plastic deformation. The formulation of the porous plasticity model is largely the same as for the metal plasticity model described above. However, the yield function in Eq. (7) is replaced by a Gurson-type yield function which introduces the void volume fraction f,

$$\Phi = \left(\frac{\varphi(\hat{\boldsymbol{\eta}})}{\sigma_M}\right)^2 + 2q_1 f \cosh\left(\frac{q_2}{2}\,\frac{\operatorname{tr}(\hat{\boldsymbol{\eta}})}{\sigma_M}\right) - \left(1 + q_3 f^2\right) \tag{13}$$

where $\sigma_M = \sigma_0 + R$.

The parameters q_1 and q_2 are calibrated from unit cell simulations, while q_3 is assumed equal to q_1^2 (Tvergaard, 1981). Like above, the associated flow rule governs plastic flow, and here the equivalent plastic strain p is obtained by

$$\hat{\mathbf{D}}_{\text{pl}} = \dot{\lambda}\,\frac{\partial \Phi}{\partial \hat{\boldsymbol{\eta}}} = \dot{p}\,\frac{\partial \Phi}{\partial \hat{\boldsymbol{\eta}}} \qquad p = \int_0^t \frac{\hat{\boldsymbol{\eta}} : \hat{\mathbf{D}}_{\text{pl}}}{(1-f)\,\sigma_M}\,\mathrm{d}\tau \tag{14}$$

The same loading–unloading conditions as in Eq. (12) apply.

The void evolution $\dot{f}$ of the material is governed by two mechanisms, where the first is enlargement of existing voids $\dot{f}_{\text{g}}$, and the second is nucleation of new voids $\dot{f}_{\text{n}}$. The total void evolution $\dot{f}$ is then

$$\dot{f} = \dot{f}_{\text{g}} + \dot{f}_{\text{n}} \tag{15}$$

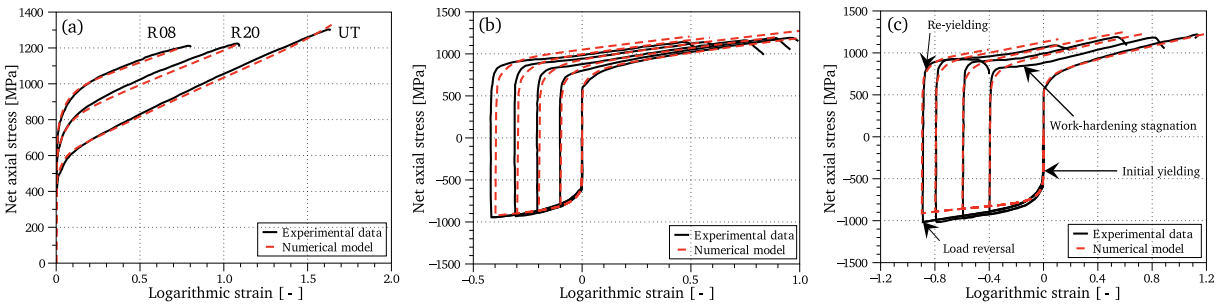

Fig. 3. Plots of experimental data compared with numerical results using the combined hardening for (a) tension tests, (b) D1 compression–tension tests and (c) D2 compression–tension tests.

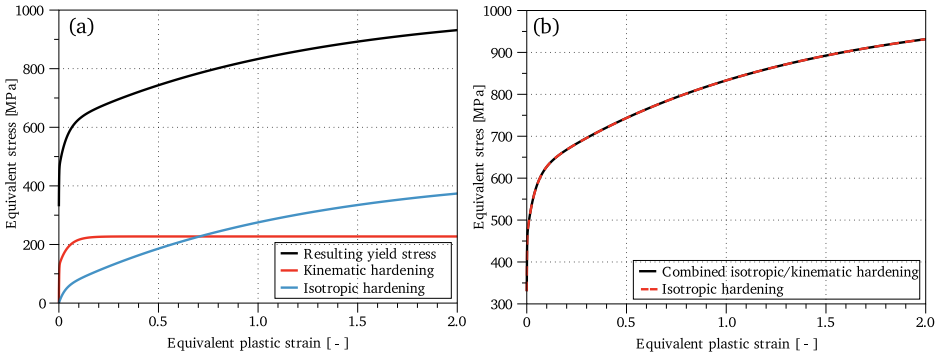

Fig. 4. Plots of resulting equivalent stress vs. equivalent plastic strain, where (a) shows the combined hardening decomposed into the kinematic and isotropic parts, while (b) shows the combined hardening together with the purely isotropic hardening.

The volumetric part of $\hat{\mathbf{D}}_{\mathrm{pl}}$ accounts for the void growth $\dot{f}_{\mathrm{g}}$, while the nucleation rate $\dot{f}_{\mathrm{n}}$ is proportional to the equivalent plastic strain rate $\dot{p}$.

Three different cases for $\dot{f}$ are investigated in this study. The first case **a** considers growth through dilatation only, which requires an initial porosity f_0. Case **b** assumes a nucleation rate $\dot{f}_{\mathrm{n}}$ proportional to $\dot{p}$, and the final case **c** has non-zero $\dot{f}_{\mathrm{n}}$ when there is plastic straining and the major principal stress σ_1 is positive (as indicated by the Macauley brackets $\langle x\rangle = (|x| + x)/2$). Similar phenomenological void nucleation laws have been used, for instance in Zhang et al. (2000), Petit et al. (2019). In mathematical terms,

a Initial porosity $f_0 > 0$:

$$\dot{f}_{\mathrm{g}} = (1-f)\,\mathrm{tr}\left(\hat{\mathbf{D}}_{\mathrm{pl}}\right) \qquad \dot{f}_{\mathrm{n}} = 0$$

b Uniform nucleation $A_{\mathrm{n},p}$ and $f_0 = 0$:

$$\dot{f}_{\mathrm{g}} = (1-f)\,\mathrm{tr}\left(\hat{\mathbf{D}}_{\mathrm{pl}}\right) \qquad \dot{f}_{\mathrm{n}} = A_{\mathrm{n},p}\,\dot{p}\int_0^t \dot{f}_{\mathrm{n}}\,\mathrm{d}\tau \le f_{\mathrm{p}}$$

c Stress controlled nucleation $A_{\mathrm{n},\sigma}$ and $f_0 = 0$:

$$\dot{f}_{\mathrm{g}} = (1-f)\,\mathrm{tr}\left(\hat{\mathbf{D}}_{\mathrm{pl}}\right) \qquad \dot{f}_{\mathrm{n}} = A_{\mathrm{n},\sigma}\,\frac{\langle\sigma_1\rangle}{\sigma_0}\,\dot{p}\int_0^t \dot{f}_{\mathrm{n}}\,\mathrm{d}\tau \le f_{\mathrm{p}}$$

Here, f_{p} is the maximum allowed volume fraction of nucleated pores.

4. Unit cell analyses

4.1. Unit cell setup

A 2D axisymmetric unit cell model following the approach by Dæhli et al. (2016) was set up using fully integrated 4-node elements. The setup springs from the work by Koplik and Needleman (1988) assuming a regular arrangement of spherical voids or particles as sketched in Fig. 5(a), where the periodic hexagon may be approximated by a circle, thus justifying the axisymmetric unit cell model. The cell has initial and current lengths L_1 and ℓ_1, respectively, in the x_1-direction, and correspondingly in the x_2-direction as illustrated in Fig. 5(b), which also shows the FE discretisation. The mesoscopic principal strains E_{11} and E_{22}, and the equivalent strain E_{eq}, are calculated from

$$E_{11} = \ln\left(\frac{\ell_1}{L_1}\right), \qquad E_{22} = \ln\left(\frac{\ell_2}{L_2}\right), \qquad E_e = \frac{2}{3}\left|E_{22} - E_{11}\right| \tag{16}$$

while the mesoscopic stresses Σ_{11} and Σ_{22} are used to find the hydrostatic stress Σ_{h} and the equivalent stress Σ_{eq} (with $\Sigma_{33} = \Sigma_{11}$) (Koplik and Needleman, 1988)

$$\Sigma_{\mathrm{h}} = \frac{1}{3}\left(\Sigma_{22} + 2\Sigma_{11}\right), \qquad \Sigma_{\mathrm{eq}} = \left|\Sigma_{22} - \Sigma_{11}\right| \tag{17}$$

The metal plasticity model described in Section 3.2 is used for the matrix material with the different hardening models as mentioned. A linear elastic particle is placed in the centre of the model, and the particle/matrix interface is shown in Fig. 5(c). The particle is included to prevent the pore from collapsing completely during the compression phase. Previous work has shown that particles may serve as crack initiation sites as they were commonly found in the bottom of dimples (Kristoffersen et al., 2013b). For certain stress states the void volume may actually grow during compression if a particle is present (Kristoffersen et al., 2016a). The top and right boundaries of the cell are restrained to lie on the same line to retain the periodic boundaries. Hard contact without any tangential friction defines the interface between the particle and the matrix, which means that no energy is dissipated through debonding because the particles were found to be only loosely attached to the matrix in the X65 material (Kristoffersen et al., 2013b). A multi-point constraint in ABAQUS (SIMULIA, 2021) is applied to impose the stress state $T(t)$ (constant or varying) onto the cell (Faleskog et al., 1998; Dæhli et al., 2016).

4.2. Calibration of porous plasticity model

The void volume fraction results from the unit cell simulations are used to calibrate the q_i parameters in the porous plasticity model (see

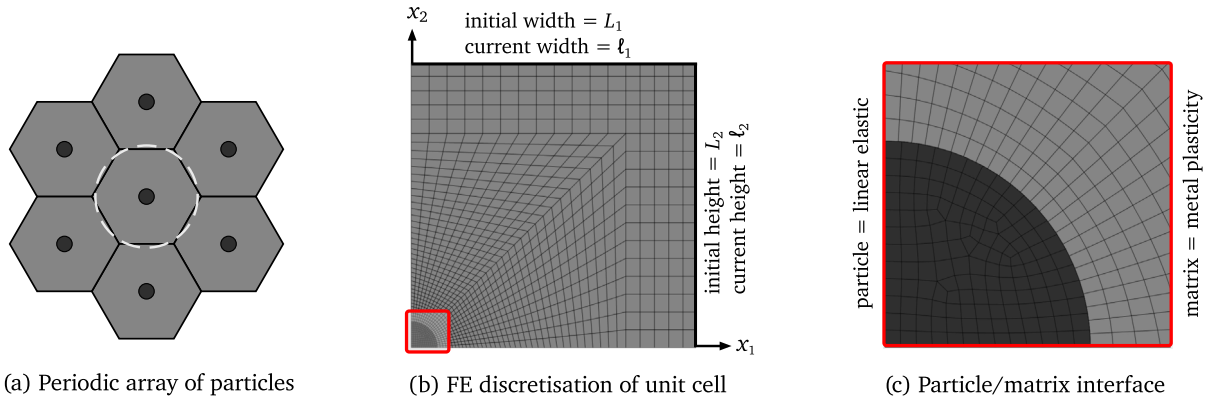

(a) Periodic array of particles (b) FE discretisation of unit cell (c) Particle/matrix interface

Fig. 5. General set up of axisymmetric unit cell simulations, where (a) shows the circular approximation to the hexagonal pattern, (b) the FE discretisation where x_1 is the radial direction and x_2 is the axis of symmetry, and (c) the particle/matrix interface.

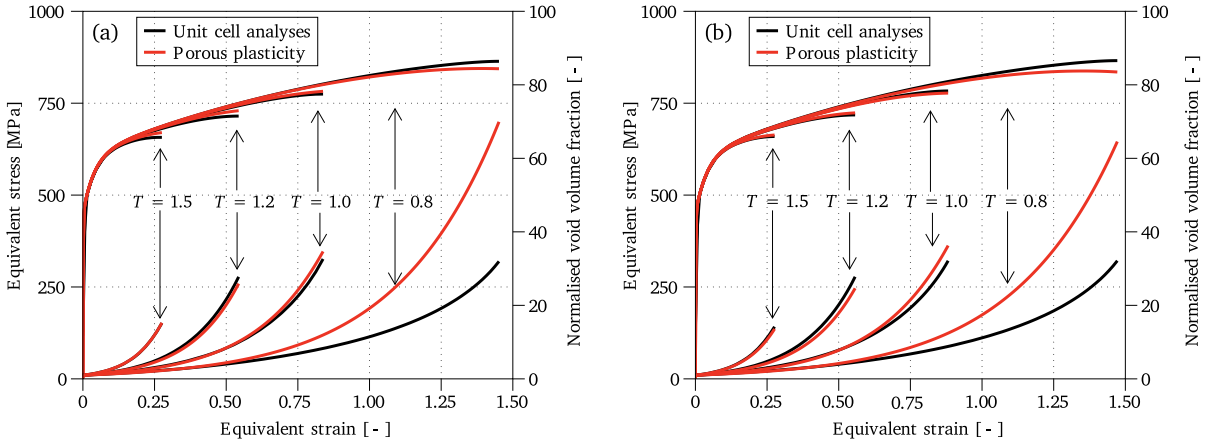

Fig. 6. Comparison between unit cell analyses and porous plasticity model for various levels of stress triaxiality T for (a) combined isotropic/kinematic hardening and (b) purely isotropic hardening.

Eq. (13)). Fig. 6 shows a comparison between the calibrated porous plasticity model and unit cell simulations for four different values of the stress triaxiality T. The results are in general very close in terms of equivalent stress as a function of the equivalent strain. For $T \geq 1.0$, the fit is very good for the void volume fraction, while for $T = 0.8$ the growth is overestimated for large values of equivalent strain (above 0.75). In general, the results match well for the combined hardening and the isotropic hardening as plotted in Fig. 6(a) and (b), respectively. The difference is small between these two cases due to the early saturation of the kinematic hardening in the combined model. The combined hardening model will be used for the localisation analyses in Section 5.

4.3. Results from monotonic loading

While the main purpose of the unit cell model is to provide data for calibration of the porous plasticity model as achieved in Fig. 6, some interesting results are noted with respect to choice of hardening model for the unit cell matrix. Results from the monotonic load cases are plotted in Fig. 7, where part (a) shows the difference between the combined hardening model and the purely isotropic hardening model. It is observed that the difference between these two is very small for the stress triaxialities simulated, i.e., $T \in \{0.8, 1.0, 1.2, 1.5\}$. The kinematic hardening part of the combined model saturates for fairly low levels of equivalent plastic strain (see Fig. 4(a)), thereby keeping the difference in response for monotonic loading low.

In addition, a pure kinematic hardening model was fitted to match the strain hardening curves from Fig. 4(b). A unit cell matrix with pure kinematic hardening was found to produce higher void growth and lower strain to failure as shown in Fig. 7(b). For $T = 0.8$, necking in the ligament (defined by the sudden increase in void volume fraction and corresponding drop in the equivalent stress in the cell) occurs at approximately 50 % higher equivalent strain for purely isotropic hardening compared with purely kinematic hardening. Increased void growth in unstrained unit cells with a purely kinematic hardening matrix was also observed by Rabold and Kuna (2005) for $T = 2.0$. In the same vein, Mear and Hutchinson (1985) obtained similar qualitative results by using the localisation framework by Rice (1976) – a kinematic hardening only material with $f_0 = 0.001$ gave similar localisation strains for plane strain tension as an isotropic hardening material with $f_0 = 0.01$, which is quite dramatic.

4.4. Results from compression–tension load

The porous plasticity model as calibrated in Fig. 6 was also subjected to non-proportional load paths in the form of compression–tension loading for comparison with unit cell results. Previous work (Kristoffersen et al., 2016a) has shown that $T \approx 0.8$ for the D2 specimens, and approximately 1.0 for the D1 specimens. The stress in the load direction (normalised by σ_0) and the strain in the loading direction are plotted in Fig. 8(a) and (b), where it is observed that the curves match very well up to the peak stress using case (a) for the void evolution. The development of the normalised void volume fraction as a function of strain in the loading direction can be seen in Fig. 8(c) and (d). For $T = 0.8$ the values deviate for large values of tensile strain

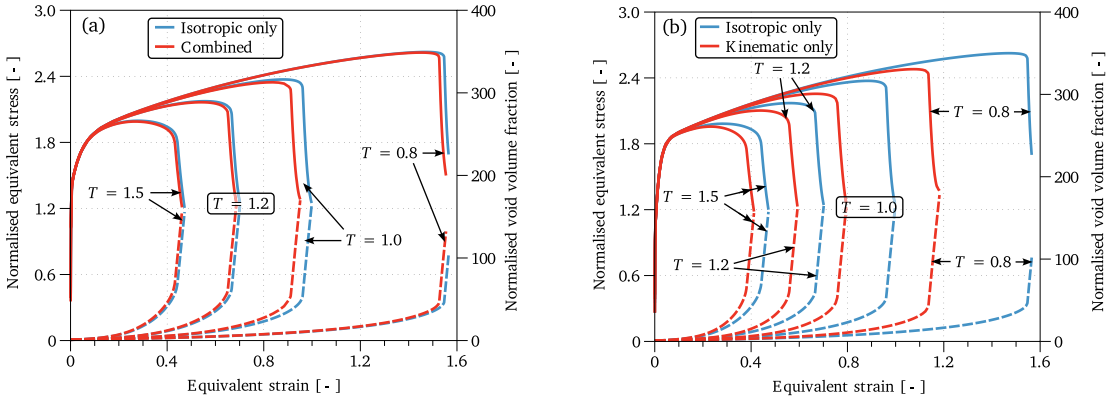

Fig. 7. Unit cell results showing the normalised equivalent stress (solid curves, normalised by σ_0) and normalised void volume fraction (dashed curves, normalised by f_0) vs. the equivalent strain, where (a) shows a comparison between the combined hardening model and the pure isotropic hardening, while part (b) illustrates the difference between using purely isotropic and purely kinematic hardening.

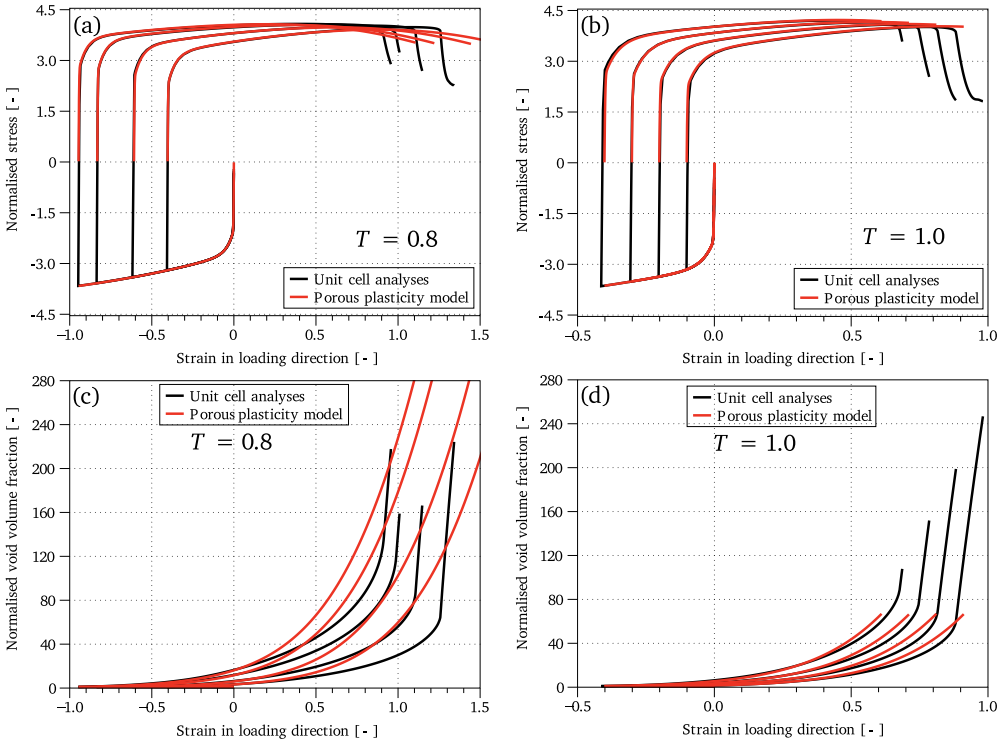

Fig. 8. Comparison between unit cell analyses (with combined hardening) and porous plasticity model for various compression–tension loading paths, where parts (a) and (b) show the stress–strain response, and parts (c) and (d) display the void volume fraction. The strain in the loading direction for the unit cells is E_{22} as defined in Eq. (16), while for the porous plasticity model it is the logarithmic strain from a single element analysis.

after compression, while for $T = 1.0$ the fit is very good up to ligament necking in the cell.

5. Localisation analyses

5.1. Framework

The localisation analyses follow the work by Marciniak and Kuczynski (1967), Yamamoto (1978), and Rice (1976). The imperfection analysis framework used in this study is described in detail by Morin et al. (2018), and only a brief summary is provided here. We assume that a thin planar imperfection band with normal unit vector $\mathbf{n}$ is present inside a homogeneously deformed solid as sketched in Fig. 9. The imperfection band is represented by the porous plasticity model (Section 3.4) and the material outside the band by the metal plasticity model (Section 3.2). We assume continuing equilibrium across the band, allowing the band normal $\mathbf{n}$ to rotate as the material deforms. Compatibility requirements across the band implies that any variation in the velocity gradient field must occur along $\mathbf{n}$. Combining compatibility and continuing equilibrium across the band leads to a system of equations to be solved (Morin et al., 2018).

The deformation of the solid is controlled by a given deformation gradient $\mathbf{F}(t)$. At some point, the porous material inside the band becomes the weaker part and the deformation inside the band increases swiftly as quantified by the ratio $\xi = \sqrt{\frac{\mathbf{D}_b : \mathbf{D}_b}{\mathbf{D} : \mathbf{D}}}$ where $\mathbf{D}$ and $\mathbf{D}_b$ are the rate-of-deformation tensors outside and inside the band, respectively. A state where a deformation increment inside the band has no corresponding deformation increment outside the band defines the onset of localisation. This depends on $\mathbf{F}(t)$ and may not happen at all. An

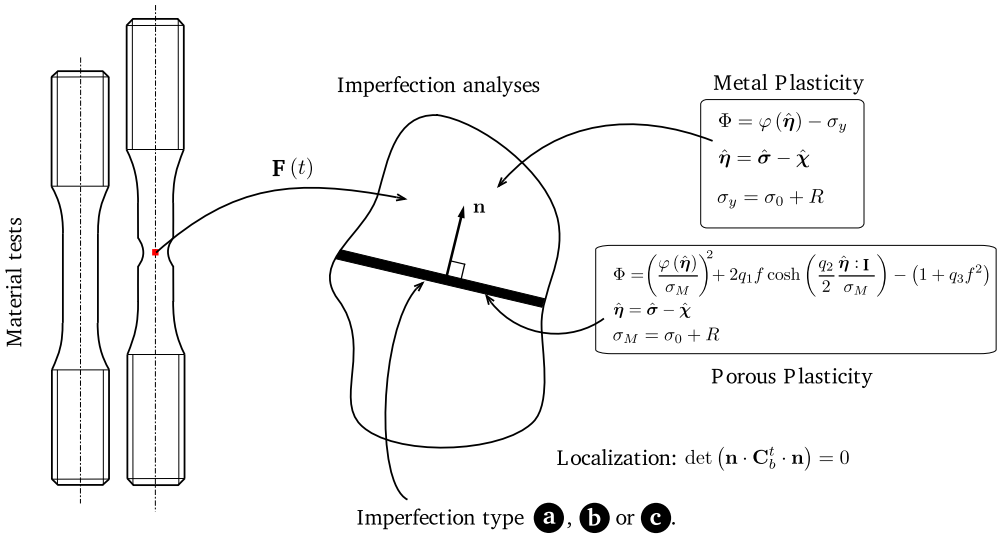

Fig. 9. Overview of the procedure for running localisation analyses with the different pore growth cases.

iterative search for the initial band normal vector $\mathbf{n}_0$ giving the lowest localisation strain is performed.

In mathematical terms, localisation occurs when the acoustic tensor $\mathbf{A}_b^t(\mathbf{n}) = \mathbf{n}\mathbf{C}_b^t\mathbf{n}$ inside the band becomes singular, i.e., $\det(\mathbf{n}\mathbf{C}_b^t\mathbf{n}) = 0$, localisation occurs. Here, $\mathbf{C}_b^t$ is the tangent modulus tensor inside the imperfection band. While this determinant goes to zero gradually, the ratio ξ rises instantly at localisation, which leads us to interpret localisation as an abrupt event for rate independent constitutive relations as used herein. When using the deformation gradient directly from an FE analysis, it is important to check for any excessive deformation, distorted elements, or possible hourglassing to avoid premature and erroneous predictions of localisation.

5.2. Analysis procedure and calibration

First, a metal plasticity model is calibrated according to experimental data as in Fig. 3. This metal plasticity model is then used in an FE simulation of the axisymmetric uniaxial tension specimen as illustrated to the left in Fig. 9. The deformation gradient $\mathbf{F}(t)$ is extracted from the critical centre element of the specimen and then applied to the bulk material outside the imperfection band in the localisation analyses, where the imperfection band is represented by the porous plasticity model. As the material deforms according to $\mathbf{F}(t)$, pores grow and/or nucleate inside the band due to the porous plasticity model using void evolution case a, b, or c.

Fig. 10(a) shows an axisymmetric FE analysis result of the UT specimen post necking. When the analysis reaches the point where the specimen fractured in the test, i.e., at a macroscopic logarithmic strain of $\varepsilon = 1.61$, the equivalent plastic strain p at the centre of the specimen is noted and used for calibration (see Fig. 10(b)). The imperfection size, which means f_0, $A_{n,p}$, and $A_{n,\sigma}$ for case a, b, and c respectively, is then obtained through inverse modelling with the extracted p as a target value for the point of sudden onset of localisation as shown in Fig. 10(c). The obtained values were $f_0 = 0.000735$, $A_{n,p} = 0.000700$, and $A_{n,\sigma} = 0.001275$. The effect of the maximum volume fraction of nucleated pores f_p on the failure strain was investigated for case b in Fig. 10(d), which shows that for very small values of f_p the onset of localisation is delayed. Increasing f_p beyond a certain point has no effect because failure occurs before f_n reaches f_p.

5.3. Results of localisation analyses

Fig. 11(a) shows the equivalent stress–equivalent strain response of the localisation analysis of the UT specimen. The softening inside the band is clearly observed, and the void evolution is almost identical for the three cases (see Fig. 11(b)). Case a naturally starts out with an initial void volume fraction f_0, but the two other cases quickly catch up and all three follow each other closely to failure. Parts (c) and (d) of Fig. 11 show the same data for the D1 specimen (not used in the calibration) with an applied prestrain of $\varepsilon = -0.20$. Now case a has a delayed onset of softening compared with b and c, which helps explain the results from Fig. 12. The void volume fraction for a decreases during compression, thereby delaying the increase in void volume fraction during the subsequent tension phase (shown in Fig. 11(d)). We thus want to emphasise the importance of accounting for the compressive phase – here by including uniform nucleation or stress based nucleation as also suggested by Chu and Needleman (1980). While this approach is phenomenologically motivated, previous experiments have shown particle cracking during compression, which may result in pore growth during this phase (Kristoffersen et al., 2013b; Frodal et al., 2017). Further, unit cell analyses have shown pore growth during compression for certain stress states (Kristoffersen et al., 2016a).

We observe that for monotonic loading, the fracture strain as a function of T (i.e., specimen geometry) is captured accurately for all three cases (see Fig. 12(a)), with case a being the most conservative. When using compression–tension load paths, we have seen from Fig. 11(d) that some kind of nucleation mechanism is necessary to capture the experimentally observed reduction in fracture strain arising from the initial compressive phase. For nucleation case b, voids nucleate as long as there is plastic deformation. In case c there is an additional requirement for nucleation, which is that the major principal stress σ_1 has to be positive. During compression, the magnitude of σ_1 is relatively small but might still be positive, thus generating nucleation during the precompression phase. When the load is reversed into tension and the material specimen resembles its initial shape, f is approximately the same for a while it has increased for b and c. This enables the latter two cases to capture the experimental trend quite accurately (see Fig. 12(b) and (c)). The final dip for $\varepsilon = -0.9$ is not well captured due to a change in the fracture mode (Kristoffersen et al., 2016a) which was probably caused by geometric effects. Still, the results are in very good agreement with the experimental data given that the localisation analysis tool was calibrated based on a single uniaxial tension test.

6. Case study: pipe denting problem

6.1. Background and motivation

Today and in the coming decades, steel pipelines are and will be used extensively for transporting fluids like oil and gas. Pipelines are

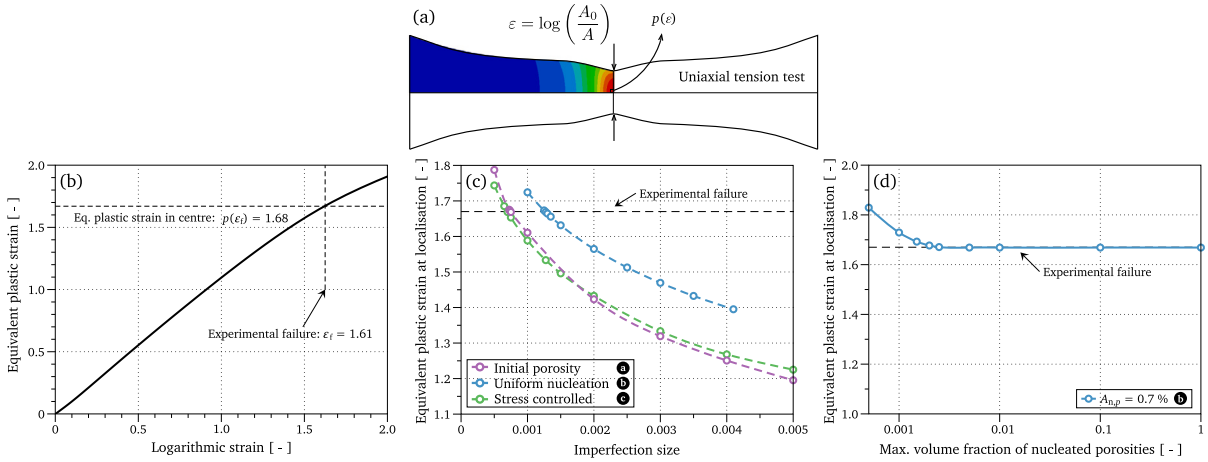

Fig. 10. Calibration of localisation analyses to experimental failure, where "imperfection size" refers to the magnitude of f_0, $A_{n,p}$, and $A_{n,\sigma}$ for cases **a**, **b**, and **c**, respectively.

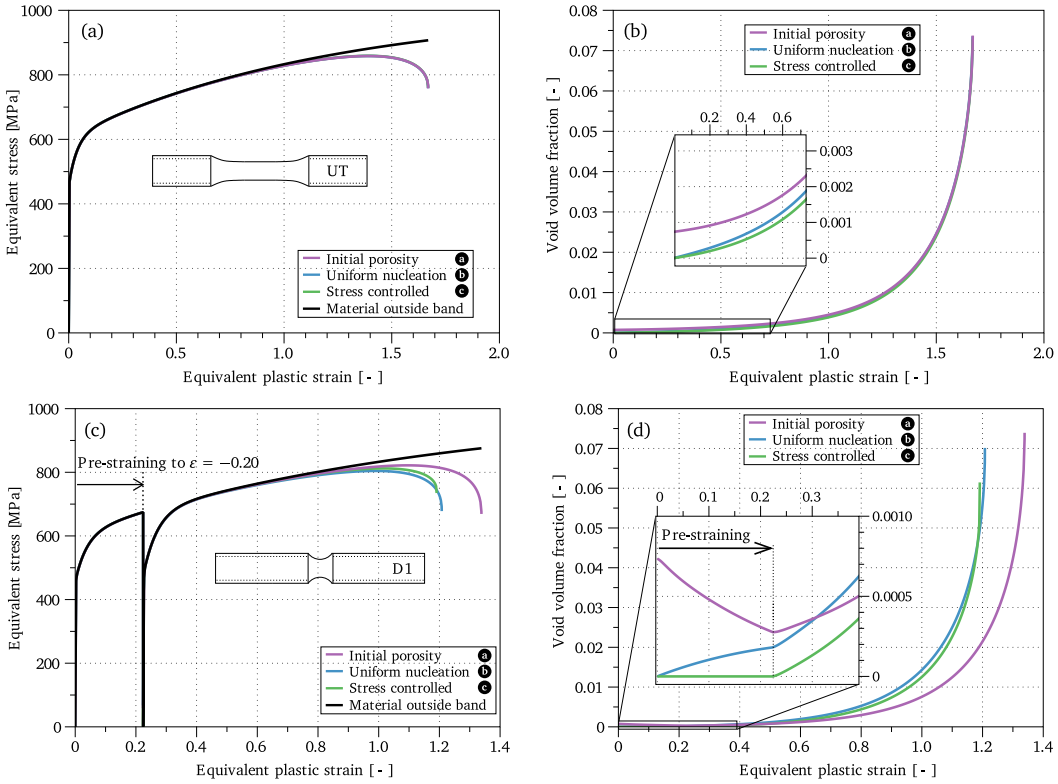

Fig. 11. Calibrated localisation analysis results for cases **a**, **b** and **c** for the UT specimen (top row), where (a) shows the equivalent stress outside and inside the imperfection band, and (b) shows the void volume fraction. The plots are recreated in (c) and (d) for the D1 specimen compressed to $\varepsilon = -0.20$. In (d), it is illustrated that the void volume fraction decreases during the compression phase for case **a**, increases for case **b**, and remains zero for case **c**. Further, the increase in void volume fraction for case **a** is delayed during the tensile phase, which in turn causes an overprediction of the fracture strain compared with the experiments.

present in many areas with high naval traffic loads, where impact and denting from e.g. anchors or trawl gear may cause severe damage (Verley et al., 1992; Gjertveit et al., 2010; Alsos et al., 2012; Vestrum et al., 2018). Pipe impact tests have shown that fracture is likely to occur directly underneath the striker during the elastic recovery after maximum displacement (Jones and Birch, 1996; Kristoffersen et al., 2016b). In this area of the pipe, the material is heavily compressed before the loading is reversed into tension – a load sequence which may cause reduction of the strain to failure and possibly ductile-to-brittle transition (Drucker et al., 1960; Kristoffersen et al., 2013b). A plausible explanation may be crease formation by self-contact due to surface instabilities during compression (Erice et al., 2020).

In this section, we ran full 3D FE simulations of the pipe denting problem described by Kristoffersen et al. (2013b) and applied the localisation analysis using the deformation gradient from the elements at the midspan cross-section where fracture was observed experimentally. This means that the deformation gradient from the material test specimen in Fig. 9 was replaced by deformation gradients from a structural component for which reliable experimental data is available. In the pipe impact simulations herein, and in instances of previous work, e.g. Kristoffersen et al. (2013a), FE simulations with commonly used fracture criteria do not indicate fracture even though the plastic deformation is reasonably well captured. This is caused by the compression–tension load sequence which reduces the relative tensile

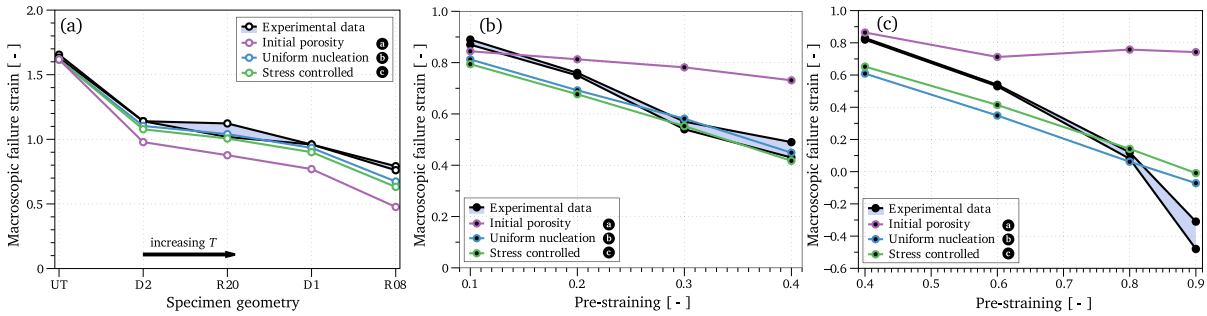

Fig. 12. Localisation results for (a) monotonic loading, (b) reversed loading from the D1 specimens, and (c) reversed loading from the D2 specimens.

strain to failure after pre-compression – an effect which increases with increasing levels of compression. The FE results from the pipe simulations – which do not give any indication of failure using standard fracture criteria – are extracted and applied in the localisation analyses. We are thus able to investigate whether the localisation analyses are able to predict the experimentally observed failure using the exact same deformation history, which would be a strong result for this approach.

We emphasise that this is not an attempt to recreate the exact experimental results, but rather a proof of concept for using the localisation analyses on a structural part and assess the qualitative features. The experiments are described in detail elsewhere (Kristoffersen et al., 2016b; Kristoffersen, 2014). A short description and a sketch of the tests – consisting of a three-point bending phase followed by a stretching phase – are included in Section 6.3.

6.2. Material and calibration

The localisation analyses discussed so far have been based on axisymmetric FE analyses. For the 3D pipe impact case a new calibration of the constants f_0, $A_{n,p}$, and $A_{n,\sigma}$ is required. Changing the element size and type generally affects fracture calibrations since larger elements typically result in smaller values for the fracture parameters. The mesh size dependency is thereby handled by the computational cell approach (Ruggieri et al., 1996), whereby the same element size is used for calibration as in the structural part. As mentioned, the "imperfection size" for the localisation analyses must be updated.

A 3D finite element model of the UT specimen from Fig. 1 was thus created in ABAQUS/Standard using 8-node linear brick elements with reduced integration and enhanced hourglass control (see Fig. 13(a) for mesh). This model was used for calibration in the same way as illustrated for the axisymmetric case in Fig. 10(a). Three symmetry planes were exploited, and the threaded area was displaced quasi-statically 1.5 mm using a smooth ramp function. The X65 pipe material is represented by a user-defined material model according to the metal plasticity model described in Section 3.2, with material constants as given in Table 1.

An element size of 0.5 mm×0.5 mm×0.5 mm was used initially as shown in Fig. 13(a). The resulting macroscopic stress–strain curve is shown in Fig. 13(c) where it is observed to diverge from the experimental curve at a logarithmic strain value of approximately 0.9. Thus, an additional simulation with an element length in the loading direction of 0.1 mm was used to accommodate the severe elongation. The new discretisation was thereby able to accurately represent the material specimen up to failure, and was therefore chosen for the discretisation of the subsequent pipe denting analysis. It is important to find a suitable mesh which gives a good representation of the macroscopic stress–strain curve in Fig. 13(c) while simultaneously converging in the pipe denting simulations.

Like in Fig. 10(a) and (b), the equivalent plastic strain p in the centre element was used to calibrate the imperfection size in the localisation analyses to match the experimental value. Fig. 13 shows that a too coarse mesh may give erroneous values of p resulting in inaccurate estimates of the onset of localisation. The maximum equivalent plastic strain p_{max} from the FE analyses was almost twice as large for the fine discretisation after displacing the threaded part of the specimen 1.5 mm as shown in Fig. 13(b). Localisation analyses using each of the cases **a**, **b** and **c** were then run with the deformation gradient from the centre element in the tension test using an element size of 0.5 mm×0.5 mm×0.1 mm. To produce an equivalent plastic strain of $p = 1.51$ at localisation, the imperfection sizes obtained were $f_0 = 0.0223$, $A_{n,p} = 0.0327$ and $A_{n,\sigma} = 0.0193$ for **a**, **b** and **c**, respectively. Symmetry conditions were used to minimise the number of initial band orientations $\mathbf{n}_0$ to be analysed. These values are more than one order of magnitude higher than what was obtained for the axisymmetric simulations (cf. Fig. 10(c)) because of the comparatively coarse mesh. Additionally, these values refer to a thin porous band inside each element, thus providing some justification for the large imperfection sizes obtained.

6.3. Pipe denting simulations

A simply supported cylindrical pipe is loaded quasi-statically at midspan as sketched in Fig. 14. The rigid supports are spaced 1.0 m apart and have a diameter of $d_{sup} = 50$ mm, and the pipes have an internal diameter of $d_{in} = 123$ mm. The wall thickness t_w between the supports was milled down to approximately 4 mm, while the thickness of the end sections resting on the supports retained their initial thickness of $t_{end} \approx 10$ mm. These end sections are modelled as rigid in the analysis. The indenter has a nose radius of $r_n = 10$ mm.

The deformation process was divided into three steps as illustrated in Fig. 15; (1) transverse denting, (2) unloading and damping, and 3) stretching. The total transverse deformation w in step (1) was set to 140 mm or 180 mm. To minimise dynamic effects, w was ramped up smoothly for a total duration of 400 s. This results in a slightly different deformation velocity for the two different values of w, but this is deemed negligible. The maximum time increment was set to 1.0 s to generate sufficient temporal resolution for the deformation gradient to be used in the subsequent localisation analyses. For step (2), the indenter was removed and the pipe was allowed to release its elastic energy and come to rest during 200 seconds. Finally, an axial force N_{ax}, ramped smoothly up from 0 to 700 kN (i.e., 350 kN due to symmetry) during 400 seconds, was applied in the pipe's axial direction. N_{ax} was applied at the centre of the rigid end section (illustrated by the red arrows in Fig. 14) to emulate the experimental setup (Kristoffersen et al., 2013b, 2016b). A full Newton solution technique was used to solve the equilibrium equations for all three steps while using the

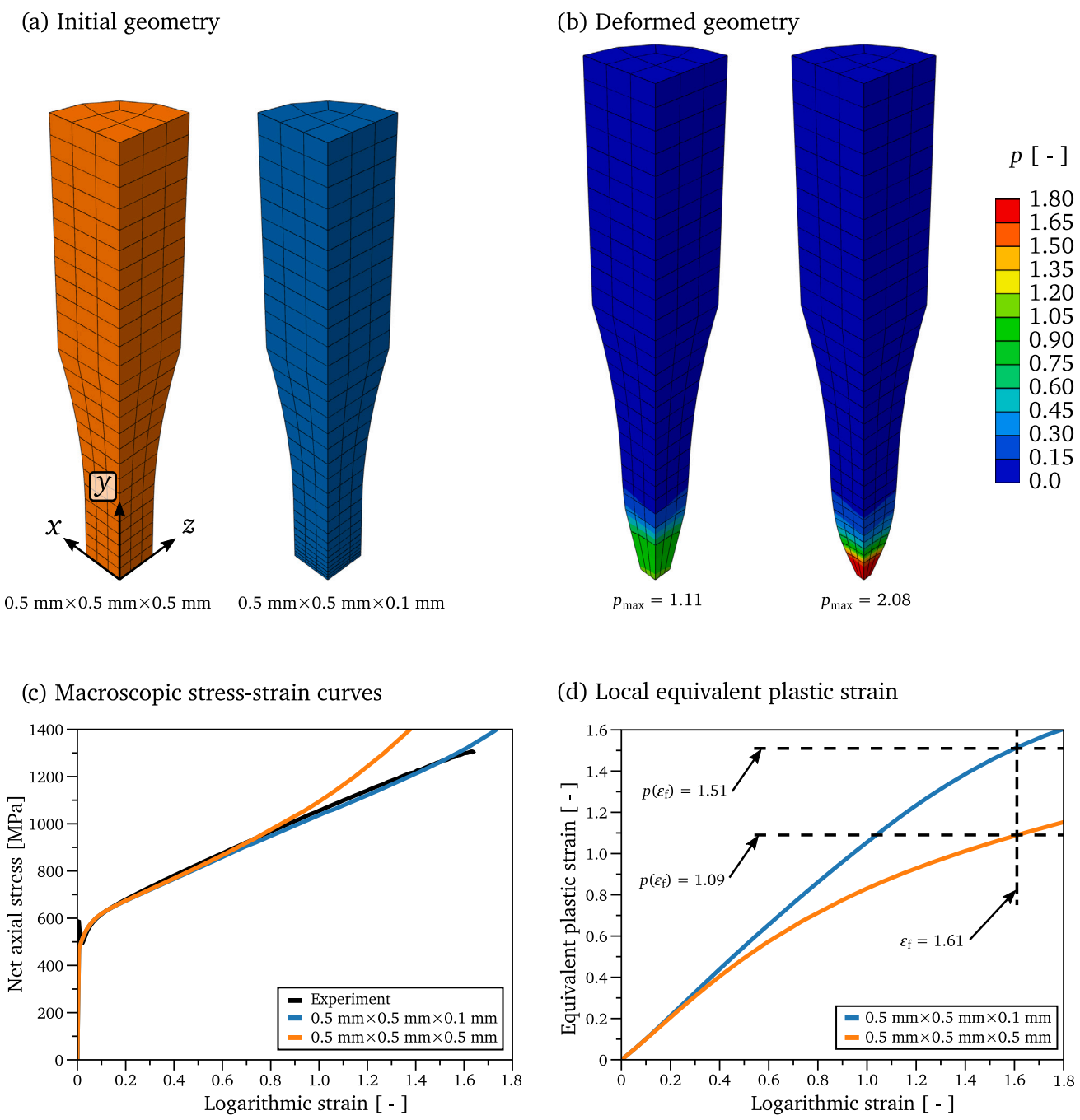

Fig. 13. FE meshes of the UT test specimen with three symmetry planes shown in (a) the undeformed configuration, and (b) the final deformed configuration with 1.5 mm shoulder displacement with the equivalent plastic strain as fringe plot. Further, part (c) shows the macroscopic stress–strain curves as measured in the tests, and (d) the equivalent plastic strain in the centre element of the specimen as a function of the measured logarithmic strain (average over the minimum cross-section).

Hilber–Hughes–Taylor method (Hilber et al., 1977) for implicit time integration.

Like the UT specimen in Fig. 13(a), the pipe was discretised in ABAQUS/Standard by 8-node linear brick elements with reduced integration and enhanced hourglass control. Only half the pipe circumference and half the pipe length were modelled, thus utilising two planes of symmetry as shown in Fig. 16. Two elements are used across the pipe thickness, but this is refined to eight elements in the denting zone resulting in an element size of approximately 0.5 mm across the thickness. The same element size is used in the circumferential direction, thus resulting in an element size in the dent zone of $0.5 \times 0.5 \times 0.1$ mm. The element size in the axial and main loading direction increases from 0.1 mm (at the symmetry plane) to 0.5 mm over the same distance (2.5 mm) as in the UT specimen mesh on the right in Fig. 13(a), thus keeping the element size from the calibration simulation the same as in the pipe simulation as recommended (Kofiani et al., 2013).

The indenter and the supports are analytic rigid surfaces, which have been shown to work better than discretised rigid parts for similar problems (Kristoffersen et al., 2018a). Surface-to-surface contact between the parts was enforced by the penalty method and a coefficient of friction equal to 0.4 to prevent slipping. The "stabilise" contact option was included to address the rigid body displacement modes present in the pipe model before contact is fully established.

On a global level, the simulations match the experiments well – both in terms of force–displacement and deformation of the cross-section as shown in Fig. 17. The difference in force level between the two

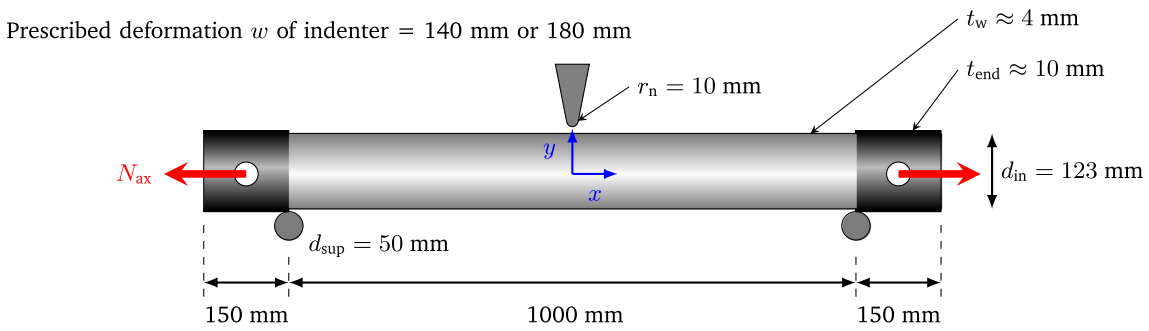

Fig. 14. Sketch of pipe denting scenario (Kristoffersen et al., 2016b).

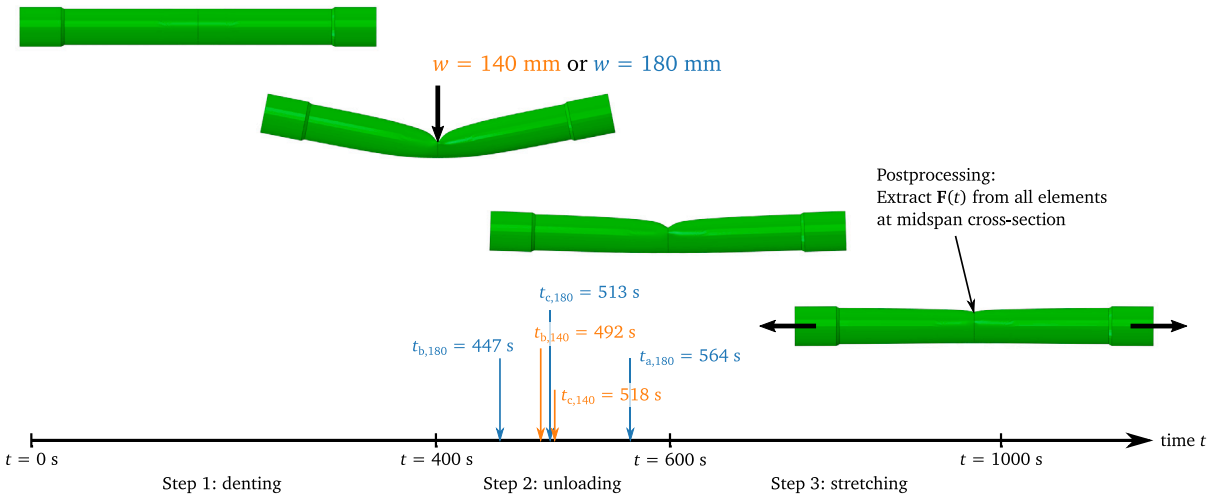

Fig. 15. All steps in FE pipe denting analyses. The time for first localisation for, say, case **c** with $w = 140$ mm, is indicated by $t_{c,140} = 518$ s and a corresponding arrow on the time axis.

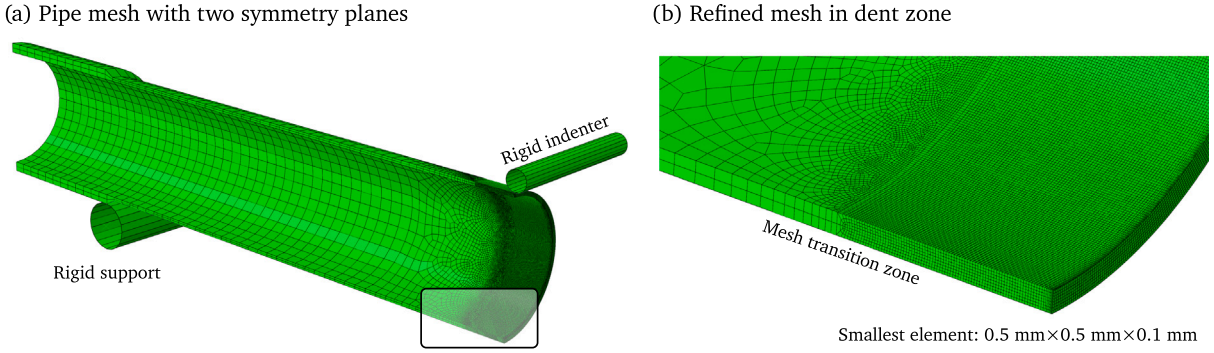

Fig. 16. FE mesh of the X65 steel pipe (a), and a close up of the refined mesh in the dent zone (b).

physical experiments is explained by their small variation in thickness resulting from the milling process (Kristoffersen et al., 2016b). Further, the force in the stretch phase is generally overestimated in the FE results herein because fracture is not accounted for. These results conform with previously obtained results using various finite element codes (Kristoffersen et al., 2014, 2013a, 2018b). It is difficult to capture this fracture accurately because of the complex load history with large compressive strains preceding tension. Well known fracture criteria like the Cockcroft–Latham (Cockcroft and Latham, 1968) or the Johnson–Cook (Johnson and Cook, 1985) criteria, which are commonly implemented in FE codes, do not properly account for possible damage accumulation during compression. A similar argument also applies to the original Gurson model (Gurson, 1977), where voids grow only under positive T as in case **a**. For this reason, the void evolution cases **b** and **c** were included in this investigation.

6.4. Localisation results

Pipe impact experiments have shown that cracks appear directly underneath the indenter at midspan, but they do not necessarily initiate at the surface – cracks may also initiate in the centre of the pipe wall (Kristoffersen et al., 2013a). For this reason, the deformation gradient $\mathbf{F}(t)$ from all the elements across the centre cross-section were used in the localisation analyses ($8 \times 410 = 3280$ elements). For each of these elements, all three void evolution cases were used.

The results are summarised in Fig. 18, where the column of plots furthest to the left shows the equivalent plastic strain at the centre

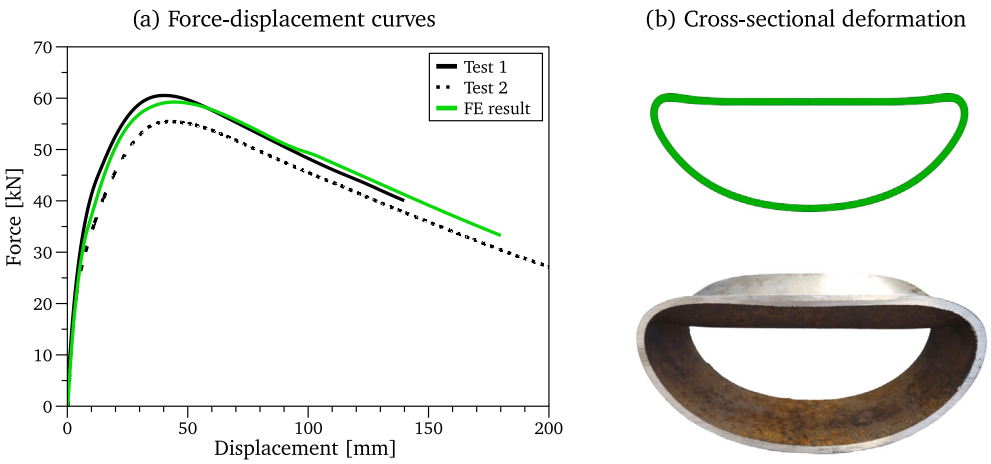

Fig. 17. Force–displacement curves of the pipe denting (a) and deformed cross-section for $w = 140$ mm (b) with experimental comparisons from Kristoffersen et al. (2016b).

cross-section of the pipe at the end of the FE analysis. While the FE analyses do not predict failure, the areas with the highest levels of equivalent plastic strain are the same areas where failure was observed in the tests. In the second column, the localisation analysis results for case **a** are shown, where no localisation is predicted for $w = 140$ mm as represented by the grey coloured dots. Like in the compression–tension load case highlighted in 11(c) and (d), voids do not grow under compression and the onset of localisation is delayed or even missed. For cases **b** and **c**, however, localisation is predicted for several elements in the same areas as observed in the experiments (Kristoffersen et al., 2013b, 2016b). Further, a clear trend emerges when increasing w to 180 mm — localisation occurs in more elements and even in the centre of the pipe wall thickness as experimentally observed (Kristoffersen et al., 2013a). For $w = 180$ mm, case **a** also gives rise to localisation.

All analyses which gave localisation for $w = 180$ mm are plotted in Fig. 19 to highlight the position and point in time localisation occurred. The angle α on the left defines the circumferential position while the colour gradient signifies from which layer of elements the localisation was predicted. The first points for onset of localisation using imperfection types **a**, **b**, and **c** were at time $t_a = 564$ s, $t_b = 447$ s and $t_c = 513$ s, respectively. All of these times are during the unloading phase as can be seen in Fig. 15 and by the red markers in Fig. 19. Again, this corresponds well with experimental observations. In all cases, localisation occurs at α between approximately 66° and 70°, which is in the area with most severe compression–tension loading. Interestingly, this happens in the outermost layer for case **c** and the innermost layer for case **b**, while for case **a** it happens on neither surface but inside the pipe wall. From Fig. 19 we observe that localisation progresses from 66° – 70° towards the 0° position during unloading, akin to the experimental behaviour.

After the tensile force is applied, localisation progresses further towards $\alpha = 0°$. This corresponds very well qualitatively with the experimental observations, where fracture was initially noted near the fold of the pipe cross-section. The crack then progressed as the pipe was straightened by the tensile force. When arriving at this point, the FE analysis will probably not provide an accurate representation of the stress state in the pipe because there is no crack in the FE analysis. In the experiments, the presence of a crack will result in lower tensile force and higher stress triaxiality (for an equivalent stretch displacement) due to a significantly reduced load-carrying area and thereby a redistribution of the stresses in the pipe wall. Nevertheless, the localisation analyses have proven to be a very useful tool for evaluating possible fracture in structures under complex loading as well as in material tests.

To highlight the differences between the three cases, results from a representative element from the $w = 180$ mm pipe denting simulation was studied in more detail. The element is located at second outermost layer at an angle $\alpha = 66.1°$, which is in the area where fracture was observed experimentally. The deformation gradient $\mathbf{F}(t)$ from this element resulted in localisation for all cases, and the stress triaxiality T and the void volume fraction inside the band as functions of the equivalent plastic strain p outside the band are plotted in Fig. 20(a) and (b), respectively. Here we observe that the stress triaxiality is positive initially when the bending is in the circumferential direction. When the pipe is bent further, the stress triaxiality becomes negative and the void volume fraction starts to decrease for case **a**. Case **c** also shows a decreasing void volume fraction, while case **b** displays a continuously increasing void volume fraction. These qualities are reflected in the equivalent plastic strain at the onset of localisation, which is highest for **a** and lowest for **b**. After load reversal, occurring at approximately $p = 0.75$, the inclination of the void volume fraction curve is notably higher for **b** and **c** compared with **a**, even though the total void volume fraction is by far the lowest for case **c** at this point.

7. Discussion

We have seen that a combined isotropic/kinematic hardening model can provide the same macroscopic stress–strain curves for uniaxial tension as purely isotropic and/or purely kinematic hardening models. When applied to unit cells, however, there is a notable increase in void growth when using kinematic hardening compared with isotropic hardening as shown in Fig. 7. Similar results were obtained in the localisation analyses by Mear and Hutchinson (1985), who found that the localisation strain was increased by approximately a factor 2 when using isotropic hardening compared with kinematic hardening for the same initial void volume fraction f_0. These results tell us that a combined isotropic/kinematic hardening model is needed and that it is important to find the correct hardening ratio. One should also be careful to interpret the void volume fraction as a quantity with a clear physical meaning. If, for instance, computed tomography is used to quantify f_0 for use in analyses of this kind, it becomes even more important to correctly model the hardening. In this study, however, f_0 is, along with $A_{n,p}$ and $A_{n,\sigma}$, treated as a model parameter to be fit to available data as exemplified by Figs. 10 and 13.

The main goal of this study was to investigate whether localisation analyses – as has been applied successfully to material tests subjected to proportional (Morin et al., 2018) and non-proportional (Morin et al., 2019) loading – were also applicable to highly non-proportional compression–tension material tests involving load reversal and structural problems with unconventional and complex load histories as suggested in Fig. 15. In short, the localisation analyses were in excellent agreement with the experimental material test data as summarised in

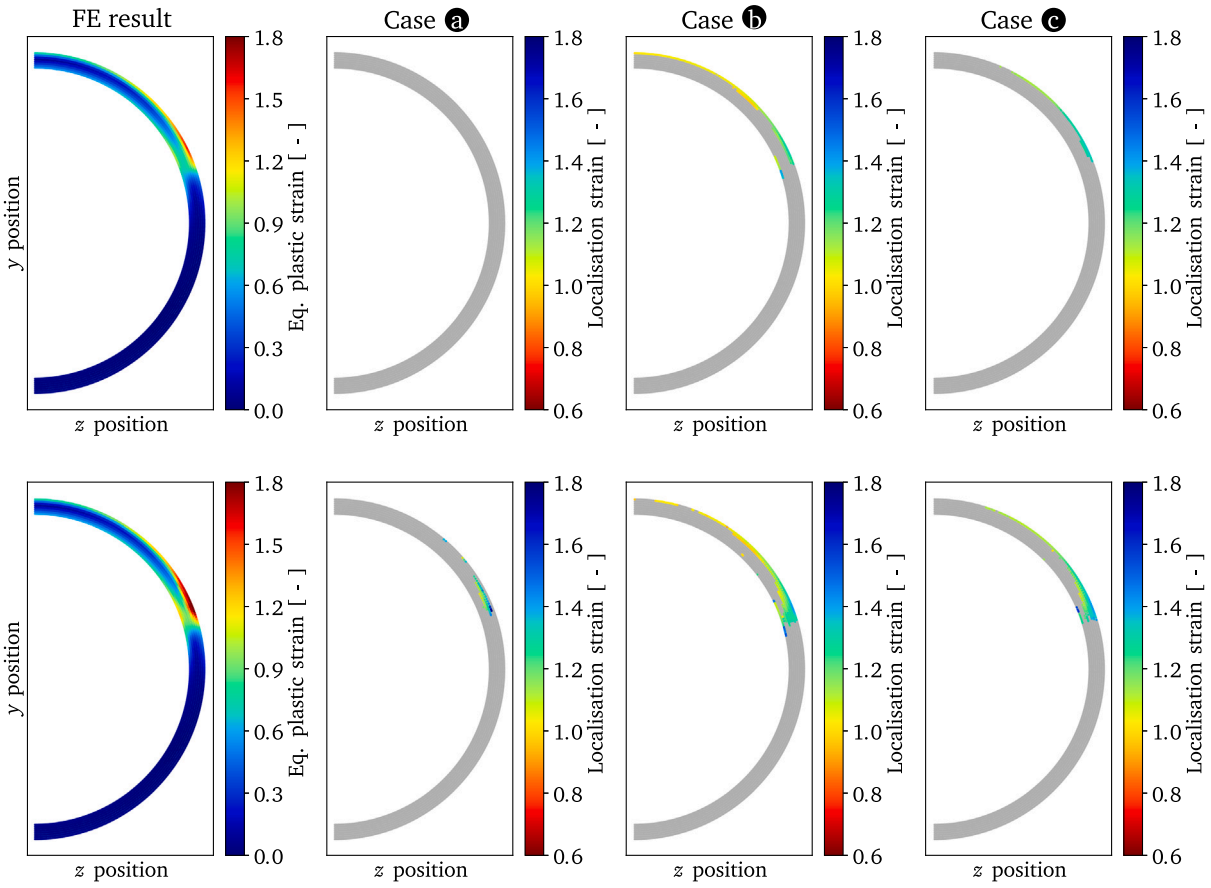

Fig. 18. Figure showing the undeformed midspan cross-section of the pipe, where the left column of plots shows the equivalent plastic strain p at the end of the FE analysis with 140 mm pipe dent (top row) and 180 mm pipe dent (bottom row). In each of the next three columns, the localisation strains as predicted by the localisation analyses are plotted, where each dot represent a separate localisation analysis. A grey coloured dot means that no localisation was predicted.

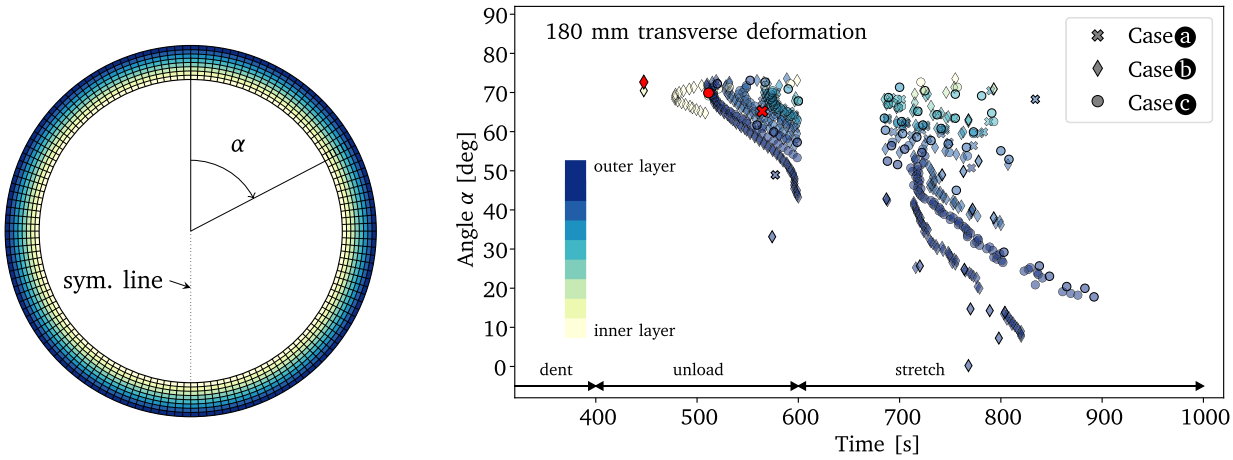

Fig. 19. All imperfection analyses which resulted in localisation in the bottom row of Fig. 18 are represented by a marker here for the three different cases. The ordinate axis indicates the position α where the onset of localisation was predicted, while the abscissa provides the time at which it occurred. The colour of the marker shows from which layer of elements localisation arised. The red markers show the first instance of localisation for each of the three cases.

Fig. 12. The analyses gave accurate results for proportional loading with very low CPU cost. Using an initial void volume fraction f_0 (case a) without any additional nucleation overpredicted the fracture strain for compression–tension loading. Based on experimental observations, compression before tension notably reduces the strain to failure and this needs to be accounted for. This was done by introducing void nucleation proportional to the equivalent plastic strain (case b) or with the added criterion that the major principal stress is positive (case c). Both of these cases were able to accurately predict the failure strain arising from compression–tension loading when the calibration was based on a single tension test only.

Applying the localisation analyses to a structural problem also gave promising results. An obvious limitation is the element size used in the structural component. Using smaller elements than herein is not

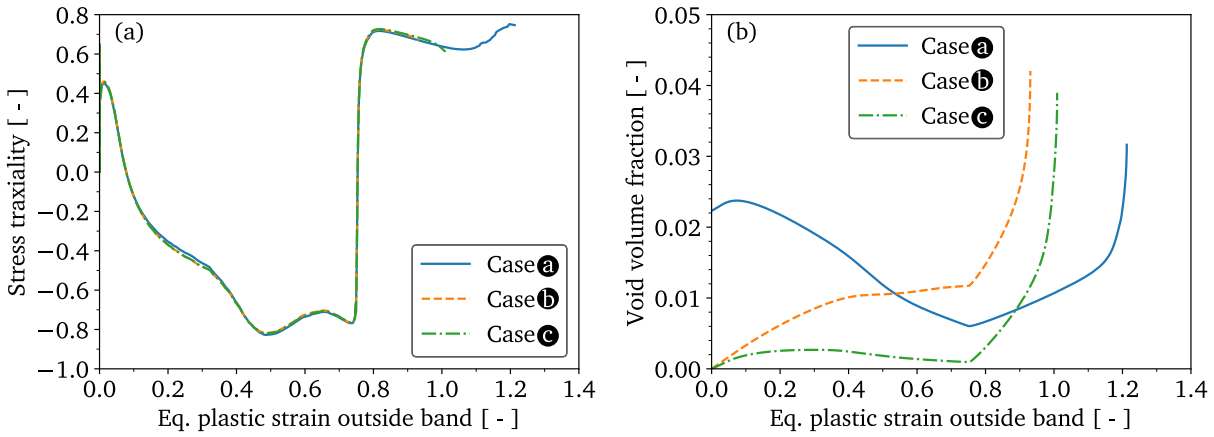

Fig. 20. Comparison of stress triaxiality (a) and void volume fraction (b) inside the imperfection band for the three void evolution cases. The analysis results are from the second outermost element at $\alpha = 66.1°$ from the $w = 180$ mm pipe denting simulation.

advisable because it caused convergence issues and will increase the simulation time further. Larger elements might deteriorate the accuracy, as illustrated in Fig. 13(c) — the accuracy of the localisation analyses are dependent on the accuracy of the underlying finite element simulation. The wall clock simulation time for the pipe simulation was about 36 h on 8 CPUs of a high-performance workstation.

While a single localisation analysis is CPU cheap, extracting the deformation gradient from 3280 elements and applying those in the localisation analysis using three different void evolution cases is CPU expensive. This results in approximately 10 000 analyses, which under the assumption of 1 min computation time accumulates to one week of CPU time (running multiple analyses in parallel would of course ameliorate this). To make things worse, this is when we know which elements to extract $\mathbf{F}(t)$ from. In the general case, one does not know where fracture initiates, thus making an in-situ localisation analysis tool of the imperfection kind implemented in a finite element framework less feasible. The results herein do, however, show that when the approximate location of first fracture is known, the imperfection analysis is a valuable post-processing tool as illustrated by Fig. 20. The bifurcation version of the localisation approach is, however, far more suitable for direct implementation in an FE analysis. In the bifurcation version, the solid is assumed homogeneous and the criterion for localisation reduces to checking whether $\det(\mathbf{n}\mathbf{C}^{t}\mathbf{n}) = 0$ irrespective of $\mathbf{F}(t)$ (Morin et al., 2018) with $\mathbf{C}^{t}$ being the tangent modulus tensor. This has been done in several studies and has been proven useful (Erice et al., 2020; Bergo et al., 2021; Espeseth et al., 2021).

Recent studies indicate that machine learning has become a popular tool for calibrating fracture models (Baltic et al., 2021; Wollenweber et al., 2023; Li et al., 2023). With an artificial neural network pretrained by using the imperfection version of localisation analyses for a wide range of load paths, an in-situ FE approach becomes far more feasible. Such tools do, powerful as they are, ultimately depend on the underlying training data, thus emphasising the value of reliable, high-quality, high-throughput data. In addition to a wide range of material tests, structural component tests may also serve as training data or validation cases. Component tests often induce other stress states and load paths than what is commonly obtained through material tests, and could thereby help extend the range of applications for these and other models.

8. Conclusions

Based on the work herein, the following conclusions are drawn.

- Isotropic hardening, kinematic hardening and combined isotropic/kinematic hardening models are all able to represent the macroscopic stress–strain curve from uniaxial tension tests, but may still result in markedly different void evolution in both unit cell analyses and localisation analyses.
- Localisation analyses of the imperfection variety capture proportional load cases very well, both qualitatively and quantitatively.
- For non-proportional load cases, particularly when compression precedes tension, letting voids grow from an initial void volume fraction is insufficient to capture the experimentally observed reduction in failure strain. Thus, void nucleation was introduced to ameliorate this problem, and the resulting computations gave very good agreement with experimental data.
- The imperfection version of the localisation analyses clearly capture the failure trends observed in a pipe denting problem. Both the location and timing for the initial and propagating fracture were well captured.

CRediT authorship contribution statement

Martin Kristoffersen: Writing – original draft, Visualization, Validation, Methodology, Investigation, Formal analysis, Conceptualization. **David Morin:** Writing – review & editing, Visualization, Software, Methodology, Formal analysis, Conceptualization. **Tore Børvik:** Writing – review & editing, Supervision, Project administration, Conceptualization. **Odd Sture Hopperstad:** Writing – review & editing, Supervision, Methodology, Conceptualization.

Declaration of competing interest

The authors declare that they have no known competing financial interests or personal relationships that could have appeared to influence the work reported in this paper.

Data availability

Data will be made available on request.

References

Alsos, H., Igland, R., Søreide, T., 2012. Evaluation of pipeline impact damage. In: Proceedings of the ASME 2012 31st International Conference on Ocean, Offshore and Arctic Engineering, Rio de Janeiro, Brazil. Paper no. 83859.

Armstrong, P., Frederick, C., 1966. A Mathematical Representation of the Multiaxial Bauschinger Effect. Technical Report, G.E.G.B. Report RD/B/N731.

Baltic, S., Asadzadeh, M.Z., Hammer, P., Magnien, J., Gänser, H.-P., Antretter, T., Hammer, R., 2021. Machine learning assisted calibration of a ductile fracture locus model. Mater. Des. 203, 109604.

Bao, Y., Wierzbicki, T., 2004. On fracture locus in the equivalent strain and stress triaxiality space. Int. J. Mech. Sci. 46, 81–98.

Barsoum, I., Faleskog, J., 2007. Rupture mechanisms in combined tension and shear – Experiments. Int. J. Solids Struct. 44, 1768–1786.
Barsoum, I., Faleskog, J., 2011. Micromechanical analysis on the influence of the Lode parameter on void growth and coalescence. Int. J. Solids Struct. 48, 925–938.
Basu, S., Benzerga, A., 2015. On the path-dependence of the fracture locus in ductile materials – experiments. Int. J. Solids Struct. 71, 79–90.
Benzerga, A., Surovik, D., Keralavarma, S., 2012. On the path-dependence of the fracture locus in ductile materials – Analysis. Int. J. Plast. 37, 157–170.
Bergo, S., Morin, D., Børvik, T., Hopperstad, O.S., 2021. Micromechanical modelling of ductile fracture in pipeline steel using a bifurcation-enriched porous plasticity model. Int. J. Fract. 227, 57–78.
Bridgman, P., 1943. Internal ductile failure mechanisms in steel cold heading process. Trans. Am. Soc. Met. 38, 553–574.
Chouksey, M., Basu, S., 2021. Exploration of subsequent yield surfaces through unit cell simulations. Int. J Solids Struct. 219-220, 11–22.
Chouksey, M., Keralavarma, S.M., 2022. Ductile failure under non-proportional loading. J. Mech. Phys. Solids 164, 104882.
Chu, C., Needleman, A., 1980. Void nucleation effects in biaxially stretched sheets. J. Eng. Mater. Technol. 102, 249–256.
Cockcroft, M., Latham, D., 1968. Ductility and the workability of metals. J. Inst. Met. 96, 33–39.
Dæhli, L.E.B., Børvik, T., Hopperstad, O.S., 2016. Influence of loading path on ductile fracture of tensile specimens made from aluminium alloys. Int. J Solids Struct. 88-89, 17–34.
Dæhli, L.E.B., Morin, D., Børvik, T., Hopperstad, O.S., 2018. A lode-dependent gurson model motivated by unit cell analyses. Eng. Fract. Mech. 190, 299–318.
Drucker, D., Mylonas, C., Lianis, G., 1960. Exhaustion of ductility of E-steel in tension following compressive prestrain. Weld. J. (Res. Suppl.) 39, 117–120.
Dunand, M., Mohr, D., 2014. Effect of lode parameter on plastic flow localisation after proportional loading at low stress triaxialities. J. Mech. Phys. Solids 66, 133–153.
Enami, K., 2005. The effects of compressive and tensile prestrain on ductile fracture initiation in steels. Eng. Fract. Mech. 72, 1089–1105.
Erice, B., Pérez-Martín, M.J., Kristoffersen, M., Morin, D., Børvik, T., Hopperstad, O.S., 2020. Fracture mechanisms in largely strained solids due to surface instabilities. Int. J. Solids Struct. 199, 190–202.
Espeseth, V., Morin, D., Tekoğlu, C., Børvik, T., Hopperstad, O.S., 2021. Ductile tearing of aluminium plates: experiments and modelling. Int. J. Fract. 227, 57–78.
Faleskog, J., Gao, X., Shih, C., 1998. Cell model for nonlinear fracture analysis – I. Micromechanics calibration. Int. J. Fract. 89, 355–373.
Frodal, B., Pedersen, K., Børvik, T., Hopperstad, O., 2017. Influence of pre-compression on the ductility of AA6xxx aluminium alloys. Int. J. Fract. 206, 131–149.
Ghahremaninezhad, A., Ravi-Chandar, K., 2011. Ductile failure in polycrystalline ofhc copper. Int. J. Solids Struct. 48, 3299–3311.
Gjertveit, E., Berge, J., Opheim, B., 2010. The Kvitebjørn pipeline repair. In: Offshore Technology Conference, Houston, Texas, USA. Paper no. OTC 20814.
Gurson, A., 1977. Continuum theory of ductile rupture by void nucleation and growth: Part 1 – Yield criteria and flow rules for porous ductile media. J. Eng. Mater. Technol. 99, 2–15.
Hancock, J., Brown, D., 1983. On the role of strain and stress state in ductile failure. J. Mech. Phys. Solids 31, 1–24.
Hancock, J., Mackenzie, A., 1976. On the mechanisms of ductile failure in high-strength steels subjected to multi-axial stress-states. J. Mech. Phys. Solids 24, 147–160.
He, X., Song, S., Luo, X., Liu, J., An, L., Bai, Y., 2020. Predicting ductility of Mg/SiCp nanocomposite under multiaxial loading conditions based on unit cell modeling. Int. J. Mech. Sci. 184, 105831.
Hilber, H.M., Hughes, T.J.R., Taylor, R.L., 1977. Improved numerical dissipation for time integration algorithms in structural dynamics. Earthq. Eng. Struct. Dyn. 5, 283–292.
Hill, R., 1950. The Mathematical Theory of Plasticity. Oxford University Press.
Johnson, G., Cook, W., 1985. Fracture characteristics of three metals subjected to various strains, strain rates, temperatures and pressures. Eng. Fract. Mech. 21, 31–48.
Jones, N., Birch, R., 1996. Influence of internal pressure on the impact behaviour of steel pipelines. Int. J. Press. Vessel Technol. 118, 464–471.
Kofiani, K., Nonn, A., Wierzbicki, T., 2013. New calibration method for high and low triaxiality and validation on SENT specimens of API X70. Int. J. Press. Vessels Pip. 111-112, 187–201.
Koplik, J., Needleman, A., 1988. Void growth and coalescence in porous plastic solids. Int. J. Solids Struct. 24, 835–853.
Kristoffersen, M., 2014. Impact Against X65 Offshore Pipelines (Ph.D. thesis). Norwegian University of Science and Technology.
Kristoffersen, M., Børvik, T., Hopperstad, O., 2016a. Using unit cell simulations to investigate fracture due to compression-tension loading. Eng. Fract. Mech. 162, 269–289.
Kristoffersen, M., Børvik, T., Langseth, M., Hopperstad, O., 2016b. Dynamic versus quasi-static loading of X65 steel pipes. Eur. Phys. J. – Special Top. 225, 325–334.
Kristoffersen, M., Børvik, T., Langseth, M., Ilstad, H., Levold, E., Hopperstad, O., 2013a. Damage and failure in an x65 steel pipeline caused by trawl gear impact. In: Proceedings of the ASME 2013 32nd International Conference on Ocean, Offshore and Arctic Engineering, Nantes, France. Paper no. 11277.
Kristoffersen, M., Børvik, T., Westermann, I., Langseth, M., Hopperstad, O., 2013b. Impact against X65 steel pipes – An experimental investigation. Int. J. Solids Struct. 50, 3430–3445.
Kristoffersen, M., Casadei, F., Børvik, T., Langseth, M., Hopperstad, O., 2014. Impact against empty and water-filled X65 steel pipes – Experiments and simulations. Int. J. Impact Eng. 71, 73–88.
Kristoffersen, M., Langseth, M., Børvik, T., 2018a. Combined three-point bending and axial tension of pressurised and unpressurised X65 offshore steel pipes – Experiments and simulations. Mar. Struct. 61, 560–577.
Kristoffersen, M., Olovsson, L., Børvik, T., 2018b. Pipeline fracture due to compression-tension loading caused by foreign object impact. In: Proceedings of the ASME 2018 37th International Conference on Ocean, Offshore and Arctic Engineering, Madrid, Spain. Paper no. 77964.
Li, X., Roth, C.C., Mohr, D., 2023. Neural network based rate- and temperature-dependent Hosford-Coulomb fracture initiation model. Int. J. Mech. Sci. 260, 108643.
Ludley, J., Drucker, D., 1960. A reversed-bend test to study ductile to brittle transition. Weld. J. (Res. Suppl.) 39, 543–546.
Manes, A., Porcaro, R., Ilstad, H., Levold, E., Langseth, M., Børvik, T., 2012. The behaviour of an offshore steel pipeline material subjected to stretching and bending. Ships Offshore Struct. 7, 371–387.
Marcadet, S., Mohr, D., 2015. Effect of compression-tension loading reversal on the strain to fracture of dual phase steel sheets. Int. J. Plast. 72, 21–43.
Marciniak, Z., Kuczynski, K., 1967. Limit strains in the process of stretch-forming sheet metal. Int. J. Mech. Sci. 9, 609–620.
Mear, M., Hutchinson, J., 1985. Influence of yield surface curvature on flow localization in dilatant plasticity. Mech. Mater. 4, 395–407.
Morin, D., Dæhli, L., Børvik, T., Benallal, A., Hopperstad, O., 2019. Numerical study of ductile failure under non-proportional loading. Eur. J. Mech. A Solids 74, 221–241.
Morin, D., Hopperstad, O., Benallal, A., 2018. On the description of ductile fracture in metals by the strain localization theory. Int. J. Fract. 209, 27–51.
Oh, C.-K., Kim, Y.-J., Baek, J.-H., Kim, Y.-P., Kim, W.-S., 2007. A phenomenological model of ductile fracture of API X65 steel. Int. J. Mech. Sci. 49, 1399–1412.
Papasidero, J., Doquet, V., Mohr, D., 2015. Ductile fracture of aluminum 2024-T351 under proportional and non-proportional multi-axial loading: Bao-wierzbicki results revisited. Int. J Solids Struct. 69-70, 459–474.
Petit, T., Besson, J., Ritter, C., Colas, K., Helfen, L., Morgeneyer, T.F., 2019. Effect of hardening on toughness captured by stress-based damage nucleation in 6061 aluminum alloy. Acta Mater. 180, 349–365.
Rabold, F., Kuna, M., 2005. Cell model simulation of void growth in nodular cast iron under cyclic loading. Comput. Mater. Sci. 32, 489–497.
Rice, J., 1976. The localisation of plastic deformation. In: 14th International Congress of Theoretical and Applied Mechanics, vol. 1, pp. 207–220.
Rice, J., Tracey, D., 1969. On the ductile enlargement of voids in triaxial stress fields. J. Mech. Phys. Solids 17, 201–217.
Ruggieri, C., Panontin, T., Dodds, R., 1996. Numerical modeling of ductile crack growth in 3-D using computational cell elements. Int. J. Fract. 82, 67–95.
SIMULIA, 2021. ABAQUS user's manual version 2022.
Tekoglu, C., Hutchinson, J., Pardoen, T., 2015. On localization and void coalescence as a precursor to ductile fracture. Phil. Trans. R. Soc. A 373, 20140121.
Thomas, N., Basu, S., Benzerga, A., 2016. On fracture loci of ductile materials under non-proportional loading. Int. J. Mech. Sci. 117, 135–151.
Tvergaard, V., 1981. Influence of voids on shear band instabilities under plane strain conditions. Int. J. Fract. 17, 389–407.
Tvergaard, V., 1982. On localization in ductile materials containing spherical voids. Int. J. Fract. 18, 237–252.
Verley, R., Moshagen, B., Moholdt, N., Nygaard, I., 1992. Trawl forces on free-spanning pipelines. Int. J. Offshore Pol. Eng. 2, 24–31.
Vestrum, O., Kristoffersen, M., Polanco-Loria, M.A., Ilstad, H., Langseth, M., Børvik, T., 2018. Quasi-static and dynamic indentation of offshore pipelines with and without multi-layer polymeric coating. Mar. Struct. 62, 60–76.
Vishwakarma, V., Keralavarma, S.M., 2019. Micromechanical modeling and simulation of the loading path dependence of ductile failure by void growth to coalescence. Int. J. Solids Struct. 166, 135–153.
Voce, E., 1948. The relationship between stress and strain for homogeneous deformation. J. Inst. Met. 74, 536–562.
Wollenweber, M.A., Medghalchi, S., Guimarães, L.R., Lohrey, N., Kusche, C.F., Kerzel, U., Al-Samman, T., Korte-Kerzel, S., 2023. On the damage behaviour in dual-phase DP800 steel deformed in single and combined strain paths. Mater. Des. 231, 112016.
Yamamoto, H., 1978. Conditions for shear localization in the ductile fracture of void-containing materials. Int. J. Fract. 14, 347–365.
Yu, H., Olsen, J., He, J., Zhang, Z., 2016. Effects of loading path on the fracture loci in a 3D space. Eng. Fract. Mech. 151, 22–36.
Zhang, Z., Skallerud, B., 2010. Void coalescence with and without prestrain history. Int. J. Damage Mech. 19, 153–174.
Zhang, Z., Thaulow, C., Ødegård, J., 2000. A complete gurson model approach for ductile fracture. Eng. Fract. Mech. 67, 155–168.